

---

**1 Local wind regime induced by giant linear dunes:  
2 comparison of ERA5-Land re-analysis with surface  
3 measurements**

**4 Cyril Gadal · Pauline Delorme ·  
5 Clément Narteau · Giles F.S. Wiggs ·  
6 Matthew Baddock · Joanna M. Nield ·  
7 Philippe Claudin**

**8**  
**9 Received: DD Month YEAR / Accepted: DD Month YEAR**

**10 Abstract**

11 Emergence and growth of sand dunes results from the dynamic interaction  
12 between topography, wind flow and sediment transport. While feedbacks be-  
13 tween these variables are well studied at the scale of a single dune, the average  
14 effect of a periodic dune pattern on atmospheric flows remains poorly con-  
15 strained due to a lack of data in major sand seas. Here, we compare wind  
16 tower measurements of surface wind data to the predictions of the ERA5-  
17 Land climate reanalysis at four locations in Namibia, within and outside the  
18 giant-dune field of the Namib sand sea. In the desert plains to the north of  
19 the sand sea, observations and predictions agree well. This is also the case  
20 in the interdune areas of the sand sea during the day, but not during the  
21 night, where additional components aligned with the giant dune orientation  
22 are measured instead of the easterly wind predicted by the ERA5-Land reanal-

---

C. Gadal

Institut de Mécanique des Fluides de Toulouse, Université de Toulouse Paul Sabatier, CNRS,  
Toulouse INP-ENSEEIHT, Toulouse, France. E-mail: cyril.gadal@imft.fr

P. Delorme

Energy and Environment Institute, University of Hull, Hull, UK.

C. Narteau

Institut de Physique du Globe de Paris, Université de Paris, CNRS, Paris, France.

G. Wiggs

School of Geography and the Environment, University of Oxford, Oxford, UK.

M. Baddock

Geography and Environment, Loughborough University, Loughborough, UK.

J.M. Nield

School of Geography and Environmental Science, University of Southampton, Southampton,  
UK.

P. Claudin

Physique et Mécanique des Milieux Hétérogènes, CNRS, ESPCI Paris, PSL Research Uni-  
versity, Université de Paris, Sorbonne Université, Paris, France.

ysis. These discrepancies, with wind deviation and attenuation larger than 50° and 60 %, are linked to the daily cycle of the turbulent atmospheric boundary layer over a complex topography, and to the associated flow regimes. During the night, the low wind velocities within a shallow boundary layer induces a flow confinement, leading to a strong streamline compression above the giant dunes and thus resulting in large flow deviations. During the day, the flow confinement is reduced by higher wind velocities and deep boundary layers. We finally propose that, in multidirectional wind regimes, this mechanism and the resulting wind deflections by giant dunes could explain the occurrence of secondary dune patterns elongating in different orientations compared to the primary structures between which they develop.

**Keywords** Atmospheric boundary layer · Sand dunes · Flow over hills

---

**35 1 Introduction**

36 The description of turbulent flows over complex topography is relevant for  
37 a large variety of different environmental systems (Sherman 1978; Walmsley  
38 et al. 1982; Baines 1995; Wood 2000; Venditti et al. 2013; Finnigan et al.  
39 2020). For example, the flow over hills is of primary interest for wind power,  
40 meteorological and air pollution phenomena (Taylor et al. 1987). The proper-  
41 ties of these flows are also key to the understanding of geophysical phenom-  
42 ena, including the formation of wind-driven waves on the ocean surface (Sulli-  
43 van and McWilliams 2010), dissolution bedforms (Claudin et al. 2017; Guérin  
44 et al. 2020), or sedimentary ripples and dunes (Bagnold 1941; Charru et al.  
45 2013; Courrech du Pont 2015). Importantly, the troposphere presents a vertical  
46 structure, with a lower convective boundary layer, of typical kilometer-scale  
47 thickness, capped by a stably stratified region (Stull 1988). The largest topo-  
48 graphic obstacles, such as mountains, can therefore interact with this upper  
49 region and lead to internal wave generation or significant wind disturbances,  
50 such as lee-side downslope winds (Durran 1990).

51 Compared to mountains, aeolian sand dunes offer idealized topographies  
52 to the study of atmospheric turbulent flow over wavy bottoms, due to their  
53 smooth shape, free of canopies, resulting from their interaction with the wind  
54 (Bagnold 1941). Then, past studies have highlighted two related topographic  
55 feedbacks on the windflow close to the dune/hill surface. First is the effect  
56 on wind speed, with documented flow acceleration on upwind slopes (Weaver  
57 and Wiggs 2011) and deceleration on downwind slopes (Baddock et al. 2007),  
58 where the speed-up factor is essentially proportional to the obstacle aspect ratio  
59 (Jackson and Hunt 1975). Importantly, the velocity maximum is typically  
60 shifted upwind of the obstacle crest (Jackson and Hunt 1975; Claudin et al.  
61 2013). This behaviour has been theoretically predicted by means of asymptotic  
62 analysis of a neutrally stratified boundary-layer flow over an obstacle of  
63 vanishing aspect ratio (Jackson and Hunt 1975; Mason and Sykes 1979; Sykes  
64 1980; Hunt et al. 1988; Belcher and J.C.R. 1998). Experiments in flumes (Zilker  
65 et al. 1977; Zilker and Hanratty 1979; Frederick and Hanratty 1988; Poggi et al.  
66 2007; Bristow et al. 2022), in wind tunnels (Gong and Ibbetson 1989; Finnigan  
67 et al. 1990; Gong et al. 1996) and in field conditions at all scales (Taylor and  
68 Teunissen 1987; Claudin et al. 2013; Fernando et al. 2019; Lü et al. 2021),  
69 have also documented this effect. Interestingly, a similar behaviour exists for  
70 the pressure perturbation, but with a slight downwind shift for the pressure  
71 minimum (Claudin et al. 2021). The second effect, much less studied, is the  
72 flow deflection that occurs when the incident wind direction is not perpen-  
73 dicular to the ridge crest. While predicted to be small (less than 10°) in the  
74 linear regime valid for shallow topography (Gadal et al. 2019), significant flow  
75 steering has been reported in the field on the downwind side of steep enough  
76 obstacles, such as well-developed sand dunes (Tsoar and Yaalon 1983; Sweet  
77 and Kocurek 1990; Walker and Nickling 2002; Smith et al. 2017) and in par-  
78 ticular coastal foredunes (e.g. Rasmussen (1989), Walker et al. (2006), Walker  
79 et al. (2009), Hesp et al. (2015), Walker et al. (2017), de Winter et al. (2020)),

mountain ranges (Kim et al. 2000; Lewis et al. 2008; Fernando et al. 2019), and valley topographies (Wiggs et al. 2002; Garvey et al. 2005).

Wind measurements over sand dunes has been mainly performed over small bedforms, typically a few meters high (corresponding to tens of meters long) (e.g. Mulligan (1988), Hesp et al. (1989), Lancaster et al. (1996), Mckenna Neuman et al. (1997), Sauermann et al. (2003), Andreotti et al. (2002), Walker and Nickling (2002), Weaver and Wiggs (2011)). For practical reasons, fewer studies performed similar measurements on giant dunes (Havholm and Kocurek 1988), with kilometer-scale wavelengths and heights of tens of meters. However, they provide a choice configuration for the study of turbulent flows over a complex topography. First, one expects larger wind disturbances for larger obstacles. Secondly, their large size makes them interact with the vertical structure of the atmosphere (Andreotti et al. 2009). Third, they usually form large patterns in sand seas and thus behave as rather clean periodic perturbations, in contrast with isolated dunes. Finally, because the morphodynamics of aeolian bedforms are strongly dependent on the local wind regime (Livingstone and Warren 2019), one can expect to see the consequences of windflow disturbance by large dunes on neighbouring small dunes (Brookfield 1977; Ewing et al. 2006). A similar effect is observed on the properties of impact ripple patterns due to the presence of dunes (Howard 1977; Hood et al. 2021).

Atmospheric flows have been much studied at the desert-scale with climate reanalyses based on global atmospheric models (Blumberg and Greeley 1996; Livingstone et al. 2010; Ashkenazy et al. 2012; Jolivet et al. 2021; Hu et al. 2021), such as ERA-40, ERA-Interim or ERA-5 (Uppala et al. 2005; Dee et al. 2011; Hersbach et al. 2020). However, the spatial resolution (tens of kilometers) of these reanalyses implies average quantities that do not resolve the smaller scales of interest, which range from individual dunes to small mountains (Livingstone et al. 2010). Recently, the release of ERA5-Land has resolved this limitation by providing up to 70 years of hourly wind predictions at a 9 km spatial resolution (Muñoz-Sabater et al. 2021). However, its validity remains to be studied, especially in remote desert areas where assimilation of measured data is very low.

In this work, we compare local wind speeds and directions measured by meteorological stations at four different locations inside and north of the giant-dune field of the Namib sand sea to the regional predictions of the ERA5-Land climate reanalysis. Where the meteorological stations are surrounded by a relatively flat environment, we show that local measurements and regional predictions agree well. The agreement is also good in the interdune areas of the sand sea, except for some weak winds blowing at night, which exhibit an additional component aligned with the giant dune orientation. These winds are not predicted by the ERA5-Land reanalysis (section 2). Further, we are able to link the magnitude of these differences to the circadian cycle of the atmospheric boundary layer (section 3). Finally, we draw implications for the wind disturbances on smaller-scale dunes (section 4), suggesting a possible origin for crossing dunes.

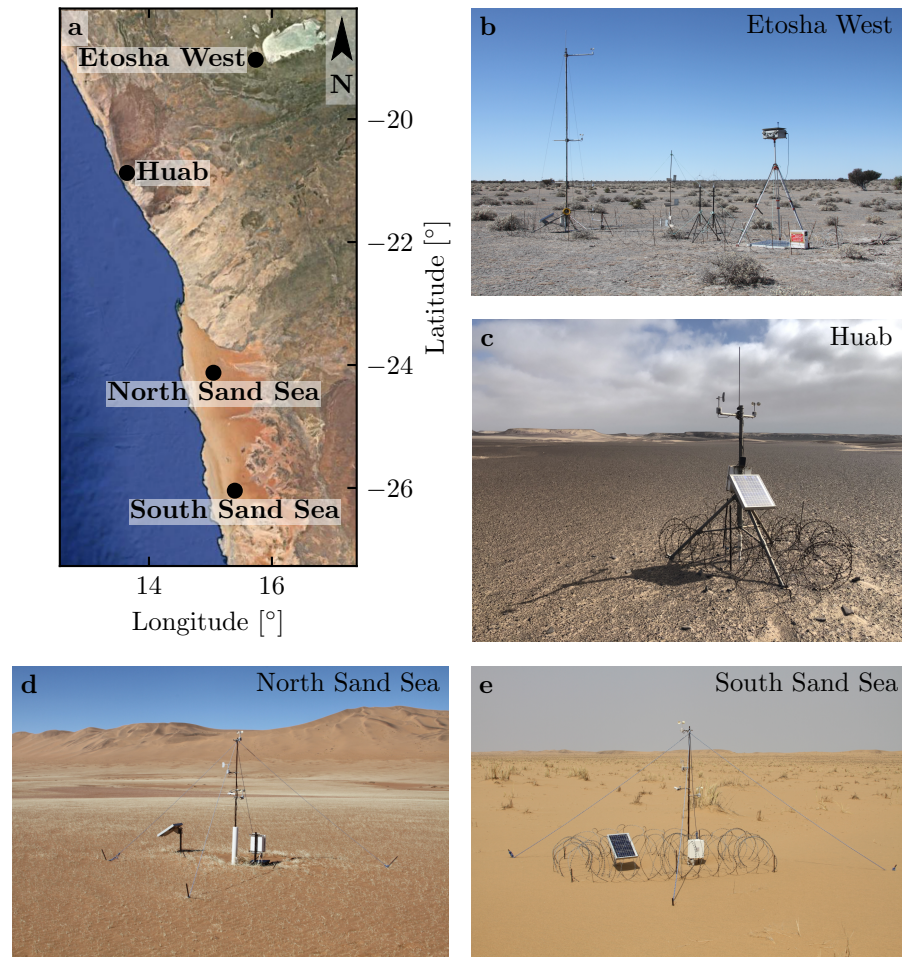


**Fig. 1** Studied field sites. **a:** Location of the different sites in Namibia. **b–e:** Photographs of the meteorological stations.

## 125 **2 Wind regimes across the Namib Sand Sea**

126 We measured the wind regime at four different locations in Namibia, represen-  
 127 tative of various arid environments across the Namib desert (Fig. 1, Fig. 2).  
 128 The Etosha West station was located at the Adamax waterhole to the west  
 129 of Etosha Pan in northern Namibia, in a sparsely vegetated area. The Huab  
 130 station was near the coast on a hyper-arid flat gravel plain lying north the  
 131 ephemeral Huab river. Here, barchan dunes up to a few meters in height de-  
 132 velop from the sediment blowing out of the river valley (Nield et al. 2017;  
 133 Hesp and Hastings 1998). These two stations were both located in relatively  
 134 flat environments. In contrast, the North Sand Sea and South Sand Sea sta-

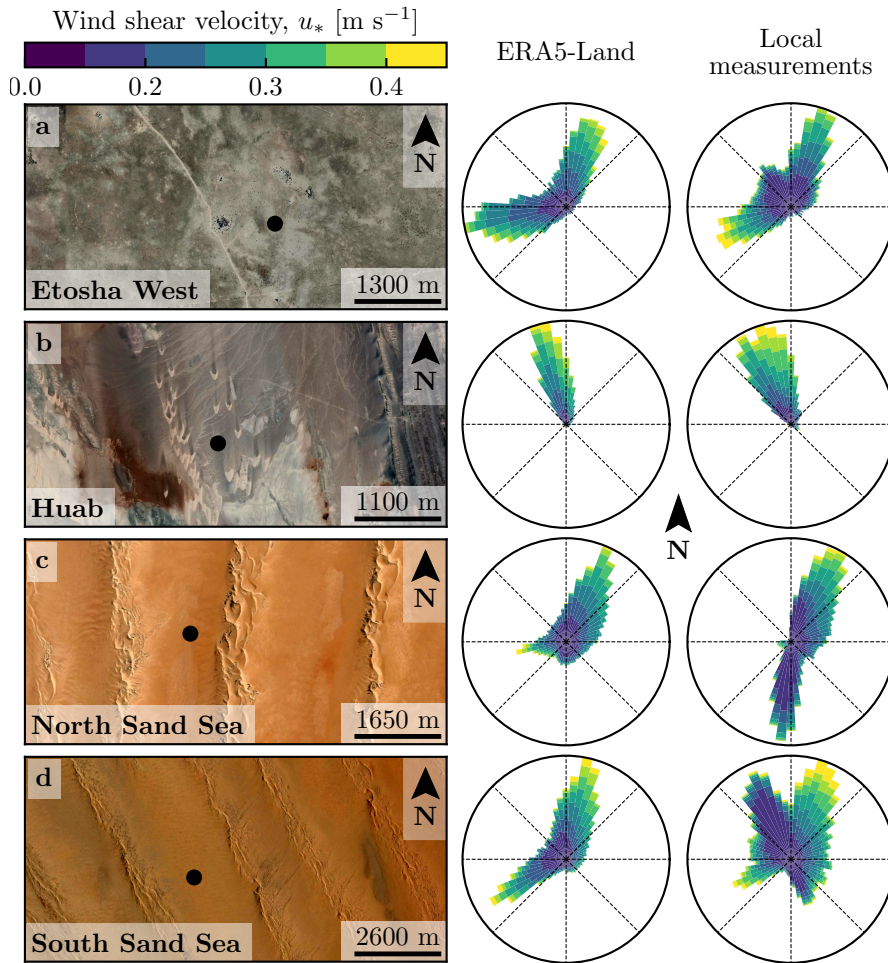


**Fig. 2** Wind data used in this study. Satellite images of these different environments (Google-Earth, Maxar Technologies, CNES/Airbus) are shown on the left. The black dots show the location of the wind measurements stations. On the center and on the right, wind roses representing the data from the ERA5-Land climate reanalysis and the local wind stations are respectively shown. Note that the bars show the direction towards which the wind blows.

tions were located in the interdunes between linear dunes with kilometer-scale wavelengths, hectometer-scale heights and superimposed patterns. In this section, we describe and compare winds from local measurements and climate reanalysis predictions.

---

139 2.1 Wind and elevation data

140 At each meteorological station (Fig. 1), wind speed and direction were sampled  
141 every 10 minutes using cup anemometers (Vector Instruments A100-LK) and  
142 wind vanes (Vector Instruments W200-P) at a single height, which was between  
143 2 m and 3 m depending on the station. The available period of measurements at  
144 each station ranged from 1 to 5 discontinuous years distributed between 2012  
145 and 2020 (Online Resource Fig. S1). We checked that at least one complete  
146 seasonal cycle was available for each station. Regional winds were extracted  
147 at the same locations and periods from the ERA5-Land dataset, which is a  
148 replay at a smaller spatial resolution of ERA5, the latest climate reanalysis  
149 from the ECMWF (Hersbach et al. 2020; Muñoz-Sabater et al. 2021). This  
150 dataset provided hourly predictions of the 10-m wind velocity and direction  
151 at a spatial resolution of  $0.1^\circ \times 0.1^\circ$  ( $\approx 9$  km in Namibia).

152 To enable direct comparison, the local wind measurements were averaged  
153 into 1-hr bins centered on the temporal scale of the ERA5-Land estimates  
154 (Online Resource Fig. S2). As the wind velocities of both datasets were pro-  
155 vided at different heights, we converted them into shear velocities  $u_*$  (Online  
156 Resource section 1), characteristic of the turbulent wind profile. Wind roses  
157 in Fig. 2 show the resulting wind data.

158 Dune properties were computed using autocorrelation on the 30-m Digital  
159 Elevation Models (DEMs) of the shuttle radar topography mission (Farr et al.  
160 2007). For the North and South Sand Sea stations, we obtain, respectively,  
161 orientations of  $85^\circ$  and  $125^\circ$  with respect to the North, wavelengths of 2.6 km  
162 and 2.3 km and amplitudes (or half-heights) of 45 m and 20 m (Online Resource  
163 Fig. S4 for more details). This agrees with direct measurements made on site.

164 2.2 Comparison of local and regional winds

165 The measured and predicted wind regimes are shown in Fig. 2. In the Namib,  
166 the regional wind patterns are essentially controlled by the sea breeze, result-  
167 ing in strong northward components (sometimes slightly deviated by the large  
168 scale topography) present in all regional wind roses (Lancaster 1985). These  
169 daytime winds are dominant during the period October-March (Fig. 3f and  
170 Online Resource Fig. 4f). During April-September, an additional (and often  
171 nocturnal) easterly component can also be recorded, induced by the combina-  
172 tion of katabatic winds forming in the mountains, and infrequent ‘berg’ winds,  
173 which are responsible for the high wind velocities observed (Lancaster et al.  
174 1984). The frequency of these easterly components decreases from inland to  
175 the coast. As a result, bidirectional wind regimes within the Namib Sand Sea  
176 and at the west Etosha site (Fig. 2a,c,d) and a unidirectional wind regime on  
177 the coast at the outlet of the Huab River (Fig. 2b) are observed.

178 In the case of the Etosha West and Huab stations, the time series of wind  
179 speed and direction from the regional predictions quantitatively match those  
180 corresponding to the local measurements (Figs. 3, 4 and Online Resource

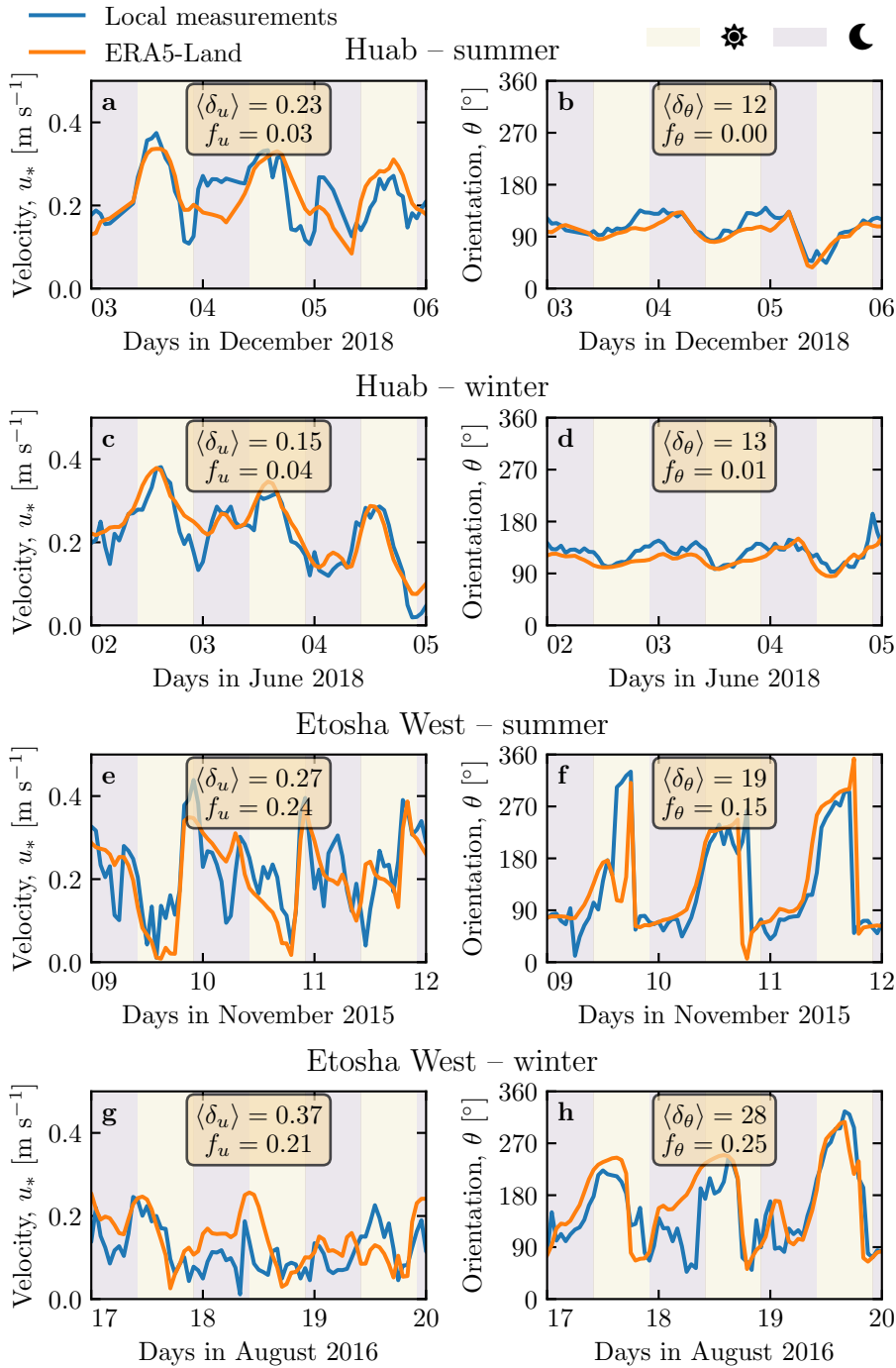


**Fig. 3** Temporal comparison between the wind data coming from the ERA5-Land climate reanalysis (orange lines) and from the local measurements (blue lines). Coloured swathes indicate day (between 1000 UTC and 2200 UTC) and night (before 1000 UTC or after 2200 UTC). Numbers indicate the average flow deflection  $\delta_\theta$  and wind modulation  $\delta_u$  over the given period, as well as the frequency of occurrence of extreme events ( $\delta_\theta > 50^\circ$ ,  $|\delta_u| > 0.6$ ). **a–b:** Huab station in summer. **b–c:** Huab station in winter. **d–e:** Etosha West station in summer. **f–g:** Etosha West station in winter. Time series of the two other stations are shown in Fig. 5.

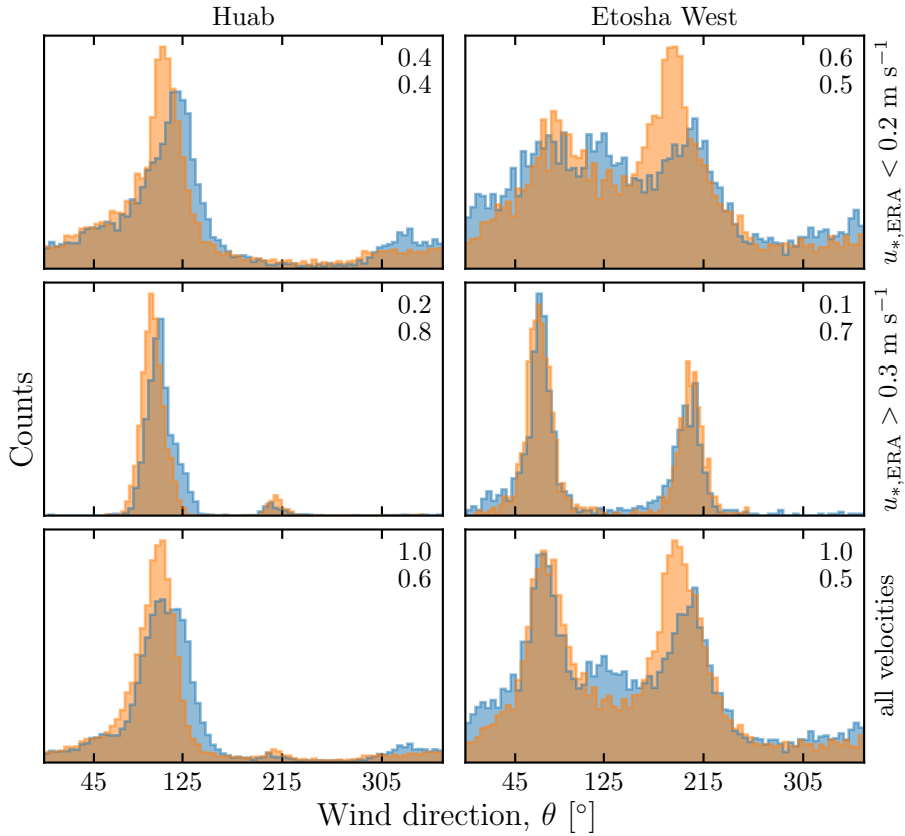


**Fig. 4** Distributions of wind direction at the Huab and Etosha West stations for the ERA5-Land climate reanalysis (orange) and the local measurements (blue). In each subplot, both distributions are plotted from the same time steps, selected with constraints on the wind wind velocity (rows) in the ERA5-Land dataset. The numbers at the top centre give the percentage of time steps selected in each sub-range, as well as the percentage of them corresponding to the day (between 1000 UTC and 2200 UTC).

181 Fig. S5). For the North Sand Sea and South Sand Sea stations within the  
 182 giant dune field, we observe that this agreement is also good, but limited to  
 183 the October-March time period (Fig. 4a, b, e, f). However, the field-measured  
 184 wind roses exhibit additional wind components aligned with the giant dune  
 185 orientation, as evidenced on the satellite images (Fig. 2c,d).

186 More precisely, during the April-September period, the local and regional  
 187 winds in the interdune match during daytime only, i.e. when the southerly/southwesterly  
 188 sea breeze dominates (Figs. 5c,d,g,h and 6). In the late afternoon and during  
 189 the night, when the easterly ‘berg’ and katabatic winds blow, measurements  
 190 and predictions differ. In this case, the angular wind distribution of the local  
 191 measurements exhibits two additional modes corresponding to reversing winds  
 192 aligned with the giant dune orientation (purple frame in Fig. 6, Online Re-  
 193 source Fig. S6). This deviation is also associated with a general attenuation

of the wind strength (Online Resource Fig. S7). Remarkably, all these figures show that these wind reorientation and attenuation processes occur only at low velocities of the regional wind, typically for  $u_{*,\text{ERA}} \lesssim 0.2 \text{ m s}^{-1}$ . For shear velocities larger than  $u_{*,\text{ERA}} \simeq 0.3 \text{ m s}^{-1}$ , the wind reorientation is not apparent. Finally, for intermediate shear velocities, both situations of wind flow reoriented along the dune crest and not reoriented can be successively observed (Online Resource Fig. S6). Importantly, these values are not precise thresholds, but indicative of a crossover between regimes, whose physical interpretation is discussed in the next section.

### 3 Influence of wind speed and circadian cycle on the atmospheric boundary layer

The wind deflection induced by dunes has previously been related to the incident angle between wind direction and crest orientation, with a maximum deflection evident for incident angles between  $30^\circ$  and  $70^\circ$  (Walker et al. 2009; Hesp et al. 2015). In the data analysed here, the most deflected wind at both the North and South Sand Sea stations is seen to be where the incident angle is perpendicular to the giant dunes (Figs. 2 and 6). It therefore appears that in our case, the incident wind angle is not the dominant control on maximum wind deflection. Further, and as shown in Fig. 6, winds of high and low velocities show contrasting behaviour in characteristics of deflection. This suggests a change in hydrodynamical regime between the winds. In this section, we discuss the relevant parameters associated with the dynamical mechanisms that govern the interactions between the atmospheric boundary layer flow and giant dune topographies. This analysis allows us to provide a physics-based interpretation of our measured wind data.

#### 3.1 Flow over a modulated bed

Taking as a reference the turbulent flow over a flat bed, the general framework of our study is understanding and describing the flow response to a bed modulation (e.g. a giant dune). Without loss of generality, we can consider in this context an idealised bed elevation in the form of parallel sinusoidal ridges, with wavelength  $\lambda$  (or wavenumber  $k = 2\pi/\lambda$ ) and amplitude  $\xi_0$ , and where the reference flow direction makes a given incident angle with respect to the ridge crest (Andreotti et al. 2012). Part of this response, on which we focus here, is the flow deflection by the ridges. In a simplified way, it can be understood from the Bernoulli principle (Hesp et al. 2015): as the flow approaches the ridge crest, the compression of the streamlines results in larger flow velocities, and thus lower pressures (Jackson and Hunt 1975). An incident flow oblique to the ridge is then deflected towards lower pressure zones, i.e towards the crest. Turbulent dissipation tends to increase this effect downstream, resulting in wind deflection along the crest in the lee side (Gadal et al. 2019).

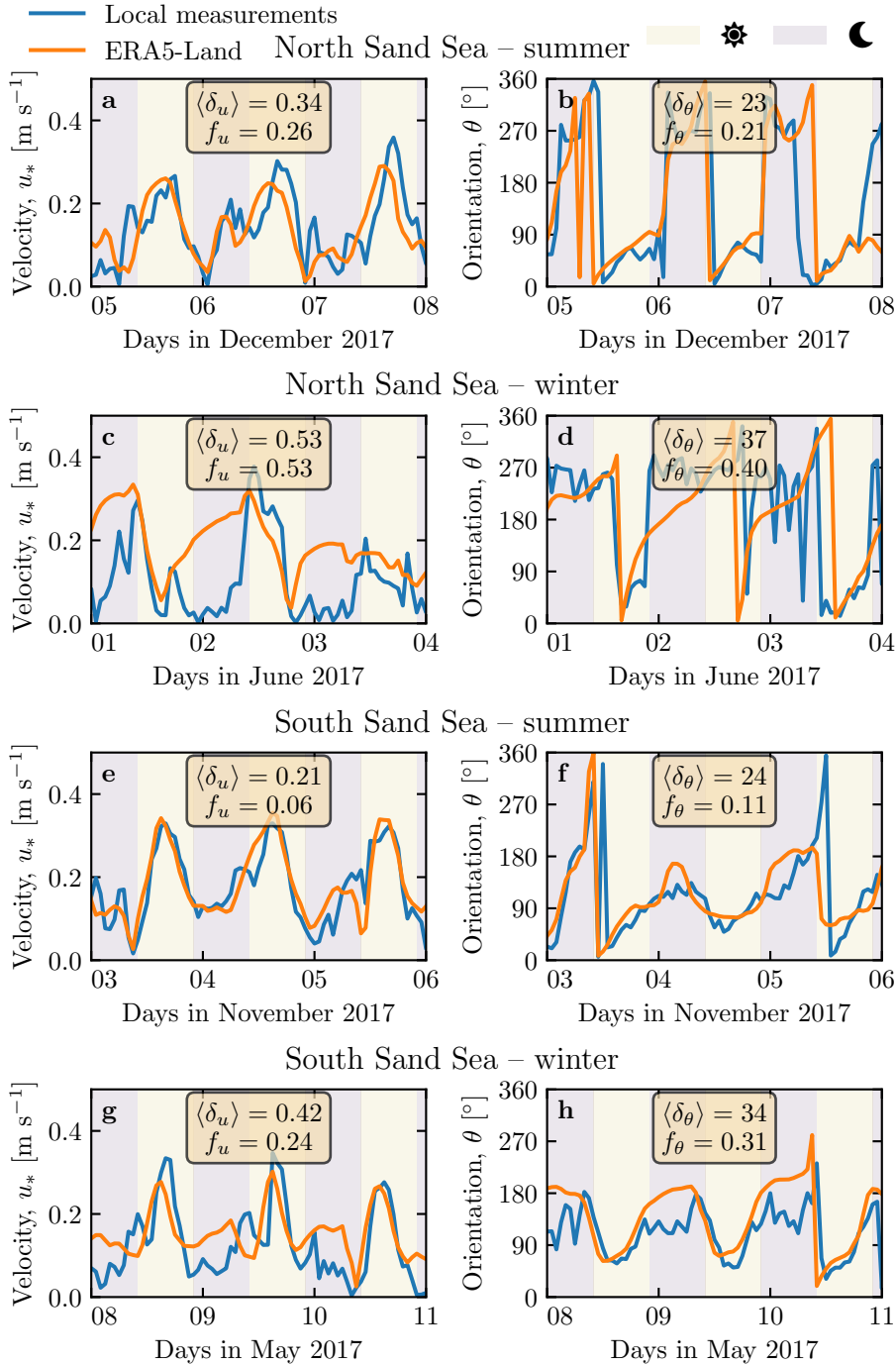


**Fig. 5** Temporal comparison between the wind data coming from the ERA5-Land climate reanalysis (orange lines) and from the local measurements (blue lines). Coloured swathes indicate day (between 1000 UTC and 2200 UTC) and night (before 1000 UTC or after 2200 UTC). Numbers indicate the average flow deflection  $\delta_\theta$  and wind modulation  $\delta_u$  over the given period, as well as the frequency of occurrence of extreme events ( $\delta_\theta > 50^\circ$ ,  $|\delta_u| > 0.6$ ). **a–b:** North Sand Sea station in summer. **b–c:** North Sand Sea station in winter. **d–e:** South Sand Sea in summer. **f–g:** South Sand Sea station in winter. Time series of the two other stations are shown in Fig. 3.

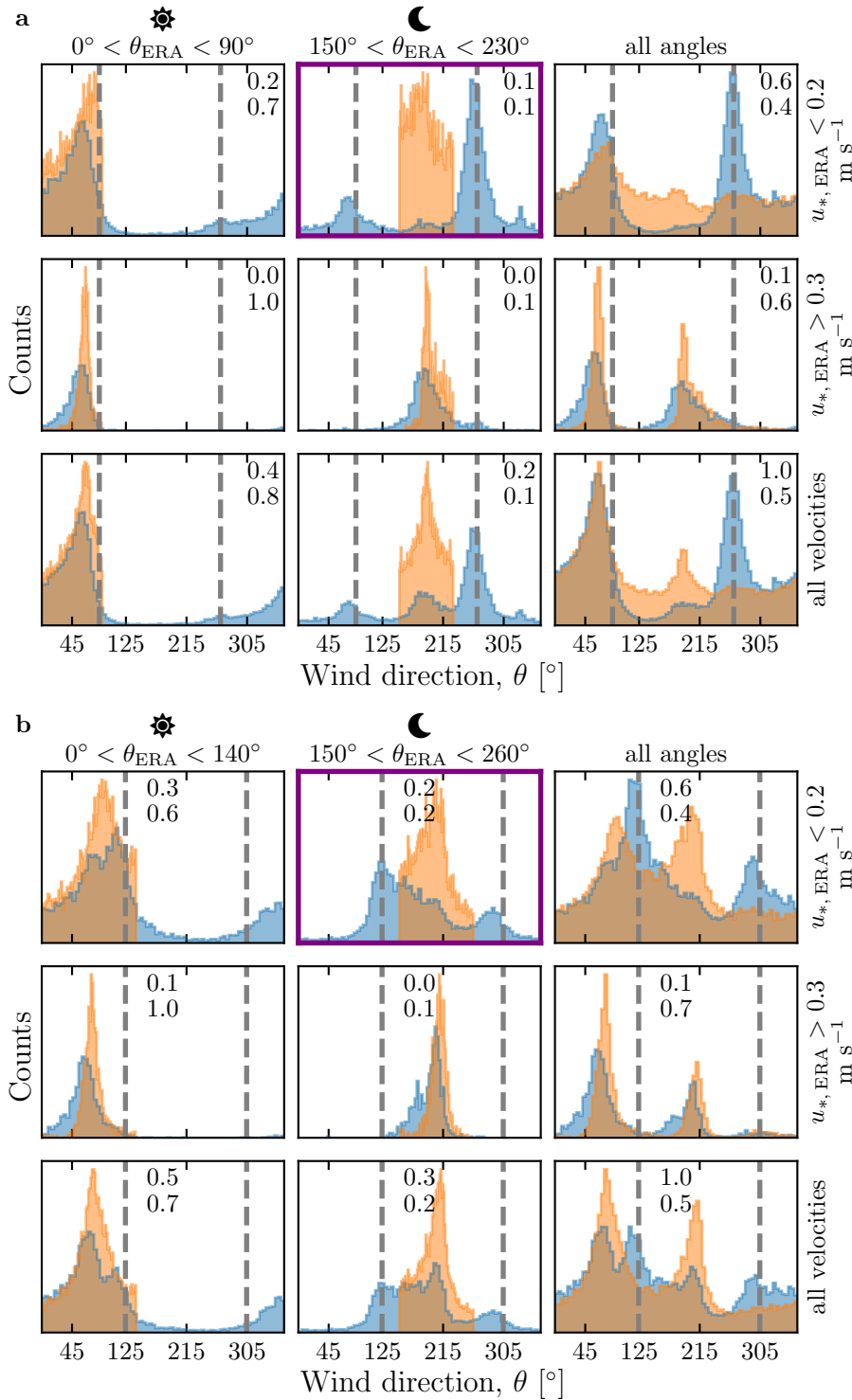


**Fig. 6** Distributions of wind direction at the North Sand Sea (**a**) and South Sand Sea (**b**) stations for the ERA5-Land climate reanalysis (orange) and the local measurements (blue). In each subplot, both distributions are plotted from the same time steps, selected with constraints on the wind direction (columns) and/or wind velocity (rows) of the ERA5-Land dataset. The grey vertical dashed lines indicate the dune orientation. The numbers at the top right give the percentage of time steps selected in each sub-range, as well as the percentage corresponding to the daytime (between 1000 UTC and 2200 UTC). Contrary to the Huab and Etosha West stations (Fig. 4), histograms does not match low wind velocities. More specifically, the purple frame highlights the regime (low wind velocities, nocturnal easterly wind) in which the data from both datasets differ.

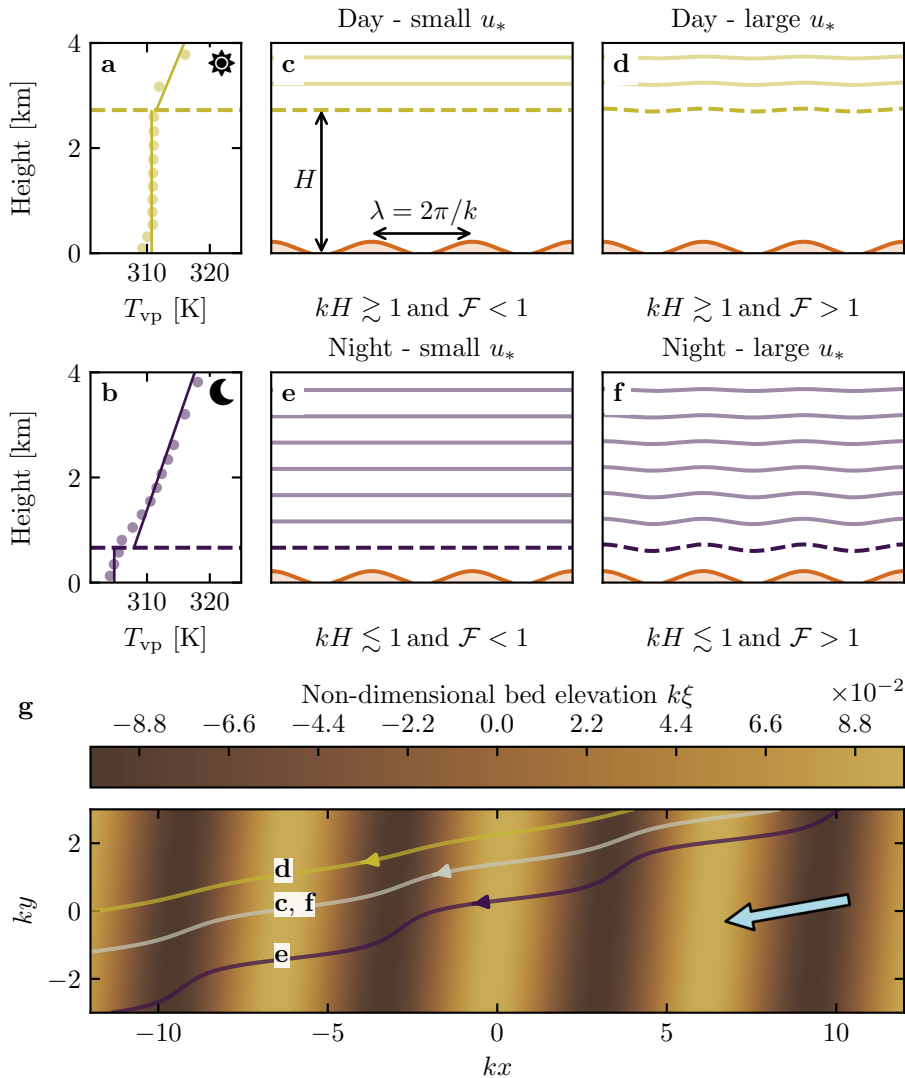


**Fig. 7** **a–b:** Vertical profiles of the virtual potential temperature at 2 different time steps (day - 03/11/2015 - 1200 UTC, night - 01/13/2013 - 0900 UTC) at the North Sand Sea station. Dots: data from the ERA5 reanalysis. Dashed lines: boundary layer height given by the ERA5 reanalysis (Online Resource section 2). Plain lines: vertical (boundary layer) and linear (free atmosphere) fits to estimate the stratification properties. **c–f:** Sketches representing the interaction between the giant dunes and the atmospheric flow for different meteorological conditions. **g:** Streamlines over a sinusoidal topography  $\xi(x, y)$  qualitatively representing the effect of low, medium and strong flow confinement, in relation to the above panels (see Appendix 1 for more details). The blue arrow indicates the undisturbed wind direction.

Flow confinement below a capping surface, which enhances streamline compression, has a strong effect on the hydrodynamic response and typically increases flow deflection. This is the case for bedforms forming in open channel flows such as rivers (Kennedy 1963; Chang and Simons 1970; Mizumura 1995; Colombini 2004; Fourrière et al. 2010; Andreotti et al. 2012; Unsworth et al. 2018). This is also relevant for aeolian dunes as they evolve in the turbulent atmospheric boundary layer (ABL) capped by the stratified free atmosphere (FA) (Andreotti et al. 2009). Two main mechanisms, associated with dimensionless numbers must then be considered (Fig. 7). First, topographic obstacles typically disturb the flow over a characteristic height similar to their length. As flow confinement is characterised by a thickness  $H$ , the interaction between the dunes and the wind in the ABL is well captured by the parameter  $kH$ . The height  $H$  is directly related to the radiative fluxes at the Earth surface. It is typically on the order of a kilometre, but significantly varies with the circadian and seasonal cycles. Emerging and small dunes, with wavelengths in the range 20 to 100 m, are not affected by the confinement, corresponding to  $kH \gg 1$ . For giant dunes with kilometric wavelengths, however, their interaction with the FA is significant (Andreotti et al. 2009). This translates into a parameter  $kH$  in the range 0.02–5, depending on the moment of the day and the season. A second important mechanism is associated with the existence of a thin intermediate so-called capping layer between the ABL and the FA. It is characterised by a density jump  $\Delta\rho$ , which controls the ‘rigidity’ of this interface, i.e. how much its deformation affects streamline compression. This is usually quantified using the Froude number (Vosper 2004; Stull 2006; Sheridan and Vosper 2006; Hunt et al. 2006; Jiang 2014):

$$\mathcal{F} = \frac{U}{\sqrt{\frac{\Delta\rho}{\rho_0} g H}}, \quad (1)$$

where  $U$  is the wind velocity at the top of the ABL and  $\rho_0$  its average density. The intensity of the stratification, i.e. the amplitude of the gradient  $|\partial_z \rho|$ , also impacts its ability to deform the capping layer under the presence of an underlying obstacle, and thus affects the influence of flow confinement. This can be quantified using the internal Froude number (Vosper 2004; Stull 2006; Sheridan and Vosper 2006; Hunt et al. 2006; Jiang 2014)  $\mathcal{F}_I = kU/N$ , where  $N = \sqrt{-g\partial_z \rho/\rho_0}$  is the Brunt-Väisälä frequency (Stull 1988). Both Froude numbers have in practice the same qualitative effect on flow confinement, and we shall restrict the main discussion to  $\mathcal{F}$  only.

With this theoretical framework in mind, and in the context of the measured wind data in the North and South Sand Sea stations, the smallest wind disturbances are expected to occur during the day, when the ABL depth is the largest and comparable to the dune wavelength ( $kH \gtrsim 1$ ), which corresponds to a weak confinement situation (Fig. 7c,d). In contrast, large wind disturbances are expected to occur during the night, when the confinement is mainly induced by a shallow ABL (Fig. 7e). However, this strong confinement can be somewhat reduced in the case of strong winds, corresponding to

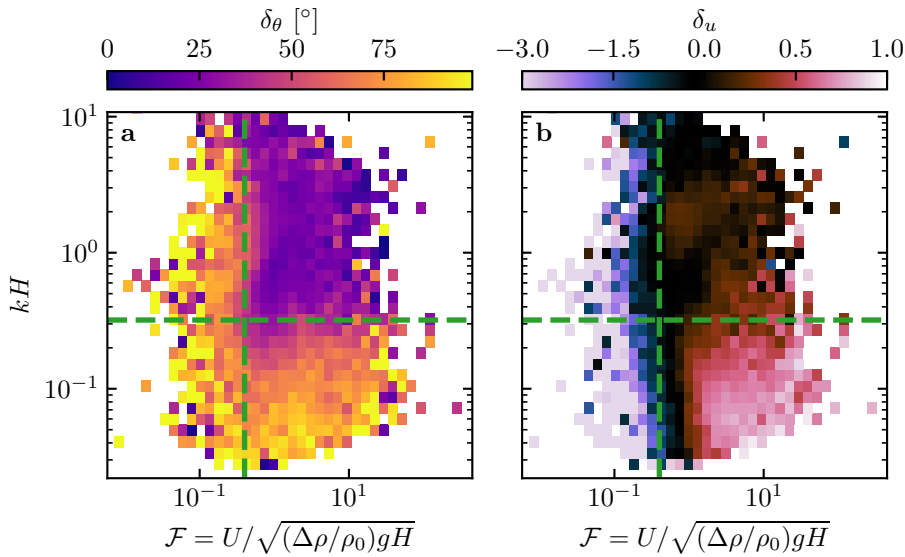


**Fig. 8** Regime diagrams of the wind deviation  $\delta_\theta$  (a) and relative attenuation/amplification  $\delta_u$  (b) in the space  $(\mathcal{F}, kH)$ , containing the data from both the North Sand Sea and South Sand Sea stations. Green dashed lines empirically delimit the different regimes. The point density in each bin of the diagrams is shown in Online Resource Fig. S10 – 95% of the data occur in the range  $-1 < \delta_u < 1$ . Similar regime diagrams in the spaces  $(\mathcal{F}_I, kH)$  and  $(\mathcal{F}_I, \mathcal{F})$  are shown in Online Resource Fig. S11.

276 large values of the Froude number and a less ‘rigid’ interface (Fig. 7f). This  
 277 is in qualitative agreement with the transition from deflected to non-deflected  
 278 winds related to low and high velocities observed in our data (Sec. 2.2).

279 **3.2 Data distribution in the flow regimes**

280 We can go one step further and analyse how our data quantitatively spread  
 281 over the different regimes discussed above. For that purpose, one needs to  
 282 compute  $kH$  and  $\mathcal{F}$  from the time series.  $H$ ,  $U$  and the other atmospheric  
 283 parameters can be deduced from the various vertical profiles (temperature,  
 284 humidity) available in the ERA5 climate reanalysis (Online Resource section  
 285 2). We quantify the flow deflection  $\delta_\theta$  as the minimal angle between the wind  
 286 orientations comparing the local measurements and the regional predictions.  
 287 We also compute the relative velocity modulation as

$$\delta_u = \frac{u_*^{\text{ERA}} - u_*^{\text{station}}}{u_*^{\text{ERA}}}. \quad (2)$$

288 These two quantities are represented as maps in the plane  $(\mathcal{F}, kH)$  (Fig. 8a,b),  
 289 and one can clearly identify different regions in these graphs. Small wind dis-  
 290 turbances (small  $\delta_\theta$  and  $\delta_u$ ) are located in the top-right part of the diagrams,

corresponding to a regime with low-interaction as well as low-confinement ( $kH$  and  $\mathcal{F}$  large enough, Fig. 7d). Lower values of  $kH$  (stronger interaction) or of Froude number (stronger confinement) both lead to an increase in wind disturbances, both in terms of orientation and velocity. Below a crossover value  $kH \simeq 0.3$ , wind disturbance is less sensitive to the  $\mathcal{F}$ -value. This is probably due to enhanced non-linear effects linked to flow modulation by the obstacle when confinement is strong. The Froude number also controls a transition from damped to amplified wind velocities in the interdune, with a crossover around  $\mathcal{F} \simeq 0.4$  (Fig. 8b). Such an amplification is rather unexpected. Checking the occurrence of the corresponding data, it appears that these amplifications are associated with the southerly sea breeze, and occur dominantly during the October-March period, when the other easterly wind is not present (Online Resource Fig. S12a–b). Furthermore, they occur less frequently during the afternoon, and more frequently at the end of the day (Online Resource Fig. S12c). This effect may be linked to a change in the flow behaviour in the lee side of the obstacles but further measurements are needed in order to assess the different possibilities (Baines 1995; Vosper 2004).

Note that, in the presented results, the only quantites depending on the choice of the hydrodynamic roughnesses (see Online Resource section 4) are the wind shear velocities, and as such the Froude number  $\mathcal{Fr}$  and the relative velocity modulation  $\delta_u$ . Considering the possible range of realistic roughnesses values ( $10^{-4}\text{m}$  to  $10^{-5}\text{m}$ ), the uncertainty of velocities estimated using the law of the wall, and thus the Froude number, is at most 30. It is harder to quantify the error on the computation of  $\delta_u$  considering the method used. However, Figure S14 shows that this choice has very little influence of the tempral variation of the relative velocity modulation, but can induce a global increase of decrease of its values. As such, it will not change the aspect of the regime diagram presented in Figure 8b, but may only change the  $\delta_u$ -value at which the transition between regimes is observed (here taken as 0, dashed black green lines in Figure 8b).

#### 321 4 Discussion and conclusion

The feedback of the giant dunes on the wind flow has important implications for smaller scales bedforms. As illustrated in Fig. 9, small linear dunes ( $\sim 50\text{ m}$  wide) are often present in the 1–2 km interdune between giant linear dunes in the Namib Sand Sea (Livingstone et al. 2010). These smaller dunes do not exhibit the same orientation as the large ones, and are sometimes named ‘crossing dunes’. Whilst differences between large and small scale dune patterns are observed ubiquitously, they are largely attributed to the presence of two different dune growth mechanisms, leading to two different dune patterns (orientations and/or morphologies) for the same wind regime (Courrech du Pont et al. 2014; Runyon et al. 2017; Lü et al. 2017; Song et al. 2019; Gadal et al. 2020; Hu et al. 2021). Here, however, our arguments enable the development of differing orientations for the small and giant linear dunes whilst also impos-

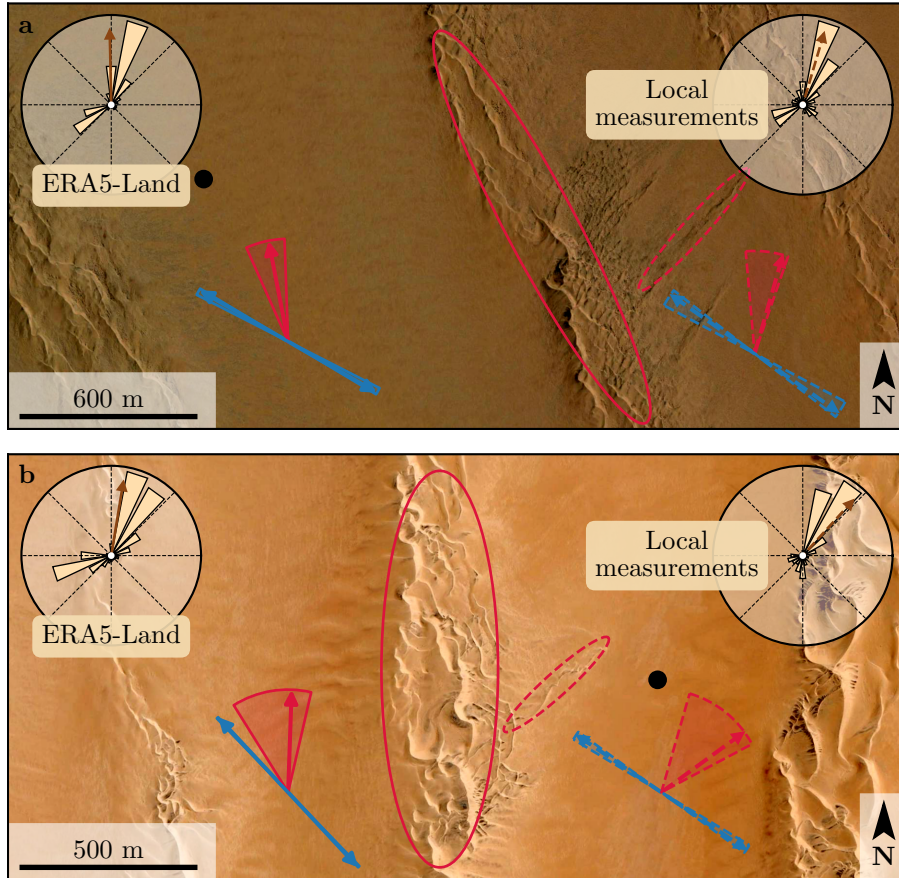


**Fig. 9** Implications for smaller scale patterns in (a) the South Sand Sea and (b) North Sand Sea. The ellipses indicate the different types of elongating dunes, at large (plain line) and small (dashed line) scales. Dune orientation are predicted using the model of Courrech du Pont et al. (2014) from the sand flux angular distributions, shown here (roses and resultant transport direction) for typical values (grain size  $180 \mu\text{m}$ , flux-up ratio of 1.6). Code for corresponding arrows: use of ERA5-Land data (plain line), use of local measurements (dashed line), prediction for the bed instability growth mechanism (blue), prediction for the elongation growth mechanism (red). Wedges show the uncertainty on the orientation calculation when parameters are varied. The black dots indicate the location of the meteorological stations with respect to the dunes. See Appendix 2 for additional details.

334 ing the same dune growth mechanism (elongating mode). Figure 9 shows how  
 335 the orientations for the small and giant dunes can be derived from the locally  
 336 measured and regionally predicted winds respectively (red arrows in Fig. 9).  
 337 These predictions require a specification for the threshold of eolian sand trans-  
 338 port. Importantly, its value expressed as a shear velocity  $u_{\text{th}} \simeq 0.15 \text{ ms}^{-1}$  is  
 339 reached in the deflected wind regime already. The feedback of the giant dunes  
 340 on the wind described in this study thus provides a potential explanation for  
 341 the existence of these small linear dunes elongating across the interdune, a

dynamic which has remained unresolved to date. These crossing dunes could provide additional constraints for the inference of local winds from bedforms, similarly to that currently performed on Mars using ripple orientations (Liu and Zimbelman 2015; Hood et al. 2021). Further work is needed to investigate these processes in more detail, including measurements of sediment transport and flow on the top of dunes.

This study presents the evidence that wind flow patterns around giant dunes are influenced by the atmospheric boundary layer, particularly during nocturnal conditions. It leaves open the debate as to whether the size of giant dunes is limited by the depth of this layer (Andreotti et al. 2009), in contrast to an unconstrained dune growth, ever-slower with size (Gunn et al. 2021a). More field evidence is needed from additional dune fields, but this mechanism would then allow for the inference of the ABL depth from giant bedform wavelengths where measurements are not feasible or available, such as Titan (Lorenz et al. 2010).

To conclude on conditions under which the ERA5-Land reanalysis data can reliably be used to study dune morphodynamics, we summarise the comparison of local (direct measurements) and regional (climate reanalysis) wind data. In flat areas, the agreement between the two confirms the ability of the ERA5-Land climate reanalysis to predict the wind regime down to scales  $\sim 10$  km, i.e. the model grid. When smaller scale topographies are present (giant dunes in our case), locally measured winds can significantly differ from the regionally predicted ones. This is the case when the disturbances induced by the dunes interact with the lower part of the ABL vertical structure, which presents circadian variations. During the day, when the capping layer is typically high, this interaction is small, and the ERA5-Land predictions are also quantitatively consistent with the local data. During the night, however, the presence of a shallow atmospheric boundary layer induces a strong confinement of the flow, and is associated with large wind deflection by the dunes. Importantly, we find that this effect can be counterbalanced for large wind velocities, which are capable of deforming the capping layer, thus decreasing the influence of the confinement.

The theoretical computation of the wind disturbances induced by sinusoidal ridges under flow confinement has been performed in the linear limit (Andreotti et al. 2009, 2012), i.e. when the aspect ratio of these ridges is small ( $k\xi_0 \ll 1$ ). These models are able to qualitatively reproduce the observed wind deflection (Appendix 1, Online Resource Figs. S11 and S13), and thus provide the physical support for the interpretation we propose here based on hydrodynamic regimes. However, these models cannot quantitatively predict the magnitude of these observations, probably due to the presence of expected non-linearities in high confinement situations linked to strong flow modulations. Besides, these linear calculations only predict wind attenuation in the interdune, in contrast with the observed enhanced velocities associated with particular evening winds from the South during the period October–March (Online Resource Fig. S12). Some other models predict different spatial flow structures in response to a modulated topography, such as lee waves and rotors

(Baines 1995; Vosper 2004). However, our measurements are located at a single point in the interdune, so we are unable to explore these types of responses. Data at different places along and across the ridges are needed to investigate and possibly map such flow structures, and for further comparisons with the models.

**Acknowledgements** We would like to acknowledge the contributors of the following open-source python libraries, Matplotlib (Hunter 2007), Numpy (Harris et al. 2020) and Scipy (Virtanen et al. 2020), which provide an incredibly efficient ecosystem allowing scientific research in Python.

All data used in this study can be found in Gadale et al. (2022). Note that it contains modified Copernicus Climate Change Service Information (2021). Neither the European Commission nor ECMWF is responsible for any use that may be made of the Copernicus Information or Data it contains. Fully documented codes used to analyse this study are available at <https://github.com/Cgadal/GiantDunes> (will be made public upon acceptance of this manuscript for publication).

Multiple grants have supported the collection of wind data through visits to the four sites between 2013 and 2020 (John Fell Oxford University Press (OUP) Research Fund (121/474); National Geographic (CP-029R-17); Natural Environment Research Council UK (NE/R010196/1 and NE/H021841/1 NSFGEO-NERC); Southampton Marine and Maritime Institute SMMI EPSRC-GCRF UK), along with research permits (1978/2014, 2140/2016, 2304/2017, 2308/2017, RPIV00022018, RPIV0052018, RPIV00230218). The authors are very grateful for support from Etosha National Park (especially Shyane Köting, Boas Erckie, Pierre du Preez, Claudine Cloete, Immanuel Kapofi, Wilferd Versfeld, and Werner Kilian), Gobabeb Namib Research Institute (Gillian Maggs-Kölling and Eugene Marais), The Skeleton Coast National Park (Joshua Kazeurua). Various researchers and desert enthusiasts have assisted with instruments and the logistics of expeditions, especially Mary Seely for expert guidance at the North Sand Sea site.

Finally, we acknowledge financial support from the Laboratoire d'Excellence UnivEarthS Grant ANR-10-LABX-0023, the Initiative d'Excellence Université de Paris Grant ANR-18-IDEX-0001, the French National Research Agency Grants ANR-17-CE01-0014/SONO and the National Science Center of Poland Grant 2016/23/B/ST10/01700.

#### Appendix 1: Linear theory of wind response to topographic perturbation

Following the work of Fourrière et al. (2010), Andreotti et al. (2012) and Andreotti et al. (2009), we briefly describe in this appendix the framework for the linear response of a turbulent flow to a topographic perturbation of small aspect ratio. As a general bed elevation can be decomposed into Fourier modes, we focus here on a sinusoidal topography:

$$\xi = \xi_0 \cos [k (\cos(\alpha)y - \sin(\alpha)x)], \quad (3)$$

which is also a good approximation for the giant dunes observed in the North Sand Sea and South Sand Sea Station (Fig. 2 and Online Resource Fig. S4). Here,  $x$  and  $y$  are the streamwise and spanwise coordinates,  $k = 2\pi/\lambda$  the wavenumber of the sinusoidal perturbation,  $\alpha$  its crest orientation with respect to the  $x$ -direction (anticlockwise) and  $\xi_0$  its amplitude. The two components of the basal shear stress  $\tau = \rho_0 u_* \mathbf{u}_*$ , constant in the flat bottom reference

<sup>432</sup> case, can then be generically written as:

$$\tau_x = \tau_0 \left( 1 + k\xi_0 \sqrt{\mathcal{A}_x^2 + \mathcal{B}_x^2} \cos [k(\cos(\alpha)y - \sin(\alpha)x) + \phi_x] \right), \quad (4)$$

$$\tau_y = \tau_0 k\xi_0 \sqrt{\mathcal{A}_y^2 + \mathcal{B}_y^2} \cos [k(\cos(\alpha)y - \sin(\alpha)x) + \phi_y], \quad (5)$$

<sup>433</sup> where  $\tau_0$  is the reference basal shear stress on a flat bed. We have defined  
<sup>434</sup> the phase  $\phi_{x,y} = \tan^{-1}(\mathcal{B}_{x,y}/\mathcal{A}_{x,y})$  from the in-phase and in-quadrature hydrodynamical coefficients  $\mathcal{A}_{x,y}$  and  $\mathcal{B}_{x,y}$ . They are functions of  $k$  and of the  
<sup>435</sup> flow conditions, i.e the bottom roughness, the vertical flow structure and the  
<sup>436</sup> incident flow direction, and the theoretical framework developed in the above  
<sup>437</sup> cited papers proposes methods to compute them in the linear regime.  
<sup>438</sup>

<sup>439</sup> Following Andreotti et al. (2012), the effect of the incident wind direction  
<sup>440</sup> can be approximated by the following expressions:

$$\mathcal{A}_x = \mathcal{A}_0 \sin^2 \alpha, \quad (6)$$

$$\mathcal{B}_x = \mathcal{B}_0 \sin^2 \alpha, \quad (7)$$

$$\mathcal{A}_y = -\frac{1}{2} \mathcal{A}_0 \cos \alpha \sin \alpha, \quad (8)$$

$$\mathcal{B}_y = -\frac{1}{2} \mathcal{B}_0 \cos \alpha \sin \alpha, \quad (9)$$

<sup>441</sup> where  $\mathcal{A}_0$  and  $\mathcal{B}_0$  are now two coefficients independent of the dune orientation  
<sup>442</sup>  $\alpha$ , corresponding to the transverse case ( $\alpha = 90^\circ$ ). In the case of a fully  
<sup>443</sup> turbulent boundary layer capped by a stratified atmosphere, these coefficients  
<sup>444</sup> depend on  $kH$ ,  $kz_0$ ,  $\mathcal{F}$  and  $\mathcal{F}_I$  (Andreotti et al. 2009). For their computation,  
<sup>445</sup> we assume here a constant hydrodynamic roughness  $z_0 \simeq 1$  mm (Online Re-  
<sup>446</sup> source section 1). For the considered giant dunes, this leads to  $kz_0 \simeq 2 \cdot 10^{-6}$ ,  
<sup>447</sup> as their wavelength is  $\lambda \simeq 2.4$  km (or  $k \simeq 2 \cdot 10^{-3}$  m<sup>-1</sup>). Values of  $z_0$  extracted  
<sup>448</sup> from field data indeed typically fall between 0.1 mm and 10 mm (Sherman and  
<sup>449</sup> Farrell 2008; Field and Pelletier 2018). Importantly,  $\mathcal{A}_0$  and  $\mathcal{B}_0$  do not vary  
<sup>450</sup> much in the corresponding range of  $kz_0$  (Fourrière et al. 2010), and the results  
<sup>451</sup> presented here are robust with respect to this choice.

<sup>452</sup> With capping layer height and Froude numbers computed from the ERA5-  
<sup>453</sup> Land time series, the corresponding  $\mathcal{A}_0$  and  $\mathcal{B}_0$  can be deduced, as displayed  
<sup>454</sup> in Online Resource Fig. S13. Interestingly, it shows similar regimes as in the  
<sup>455</sup> diagrams of Fig. 8 and Online Resource Fig. S11a,b, supporting the underlying  
<sup>456</sup> physics. However, the agreement is qualitative only. Further, the linearity  
<sup>457</sup> assumption of the theoretical framework requires  $(|\tau| - \tau_0)/\tau_0 \ll 1$ , which  
<sup>458</sup> translates into  $k\xi_0 \sqrt{\mathcal{A}_0^2 + \mathcal{B}_0^2} \ll 1$ . In our case, the giant dune morphology  
<sup>459</sup> gives  $k\xi_0 \simeq 0.1$ , which means that one quits the regime of validity of the  
<sup>460</sup> linear theory when the coefficient modulus  $\sqrt{\mathcal{A}_0^2 + \mathcal{B}_0^2}$  becomes larger than a  
<sup>461</sup> few units. In accordance with the theoretical expectations, these coefficients  
<sup>462</sup> present values on the order of unity ( $\mathcal{A}_0 \simeq 3$  and  $\mathcal{B}_0 \simeq 1$ ) in unconfined sit-  
<sup>463</sup> uations (Claudin et al. 2013; Lü et al. 2021). In contrast and as illustrated  
<sup>464</sup> in Online Resource Fig. S13a,b, larger values are predicted in case of strong

465 confinement, which does not allow us to proceed to further quantitative comparison  
466 with the data.

467 Finally, the linear model is also able to reproduce the enhancement of the  
468 flow deflection over the sinusoidal ridges when  $\sqrt{A_0^2 + B_0^2}$  is increased (Online  
469 Resource Fig. S13). Here, using  $k\xi_0 \simeq 0.1$  to be representative of the amplitude  
470 of the giant dunes at the North Sand Sea station, the coefficient modulus is  
471 bounded to 10.

## 472 Appendix 2: Sediment transport and dune morphodynamics

473 We summarise in this appendix the sediment transport and dune morphodynamics  
474 theoretical framework leading to the prediction of sand fluxes and dune  
475 orientations from wind data.

476 *Sediment transport* — The prediction of sand fluxes from wind data has been  
477 a long standing issue in aeolian geomorphological studies (Fryberger and Dean  
478 1979; Pearce and Walker 2005; Sherman and Li 2012; Shen et al. 2019). Based  
479 on laboratory studies in wind tunnels (Rasmussen et al. 1996; Iversen and  
480 Rasmussen 1999; Creyssels et al. 2009; Ho et al. 2011), as well as physical  
481 considerations (Ungar and Haff 1987; Andreotti 2004; Durán et al. 2011; Pähzt  
482 and Durán 2020), it has been shown that the steady saturated saltation flux  
483 over a flat sand bed depends linearly on the shear stress:

$$\frac{q_{\text{sat}}}{Q} = \Omega \sqrt{\Theta_{\text{th}}} (\Theta - \Theta_{\text{th}}), \quad (10)$$

484 where  $\Omega$  is a proportionality constant,  $Q = d\sqrt{(\rho_s - \rho_0)gd/\rho_0}$  is a character-  
485 istic flux,  $\Theta = \rho_0 u_*^2 / (\rho_s - \rho_0)gd$  the Shields number, and  $\Theta_{\text{th}}$  its threshold  
486 value below which saltation vanishes.  $\rho_s = 2.6 \text{ g cm}^{-3}$  and  $d = 180 \mu\text{m}$  are  
487 the grain density and diameter, and  $g$  is the gravitational acceleration. The  
488 shear velocity, and consequently the Shields number as well as the sediment  
489 flux, are time dependent.

490 Recently, Pähzt and Durán (2020) suggested an additional quadratic term  
491 in Shields to account for grain-grain interactions within the transport layer at  
492 strong wind velocities:

$$\frac{q_{\text{sat}, t}}{Q} = \frac{2\sqrt{\Theta_{\text{th}}}}{\kappa\mu} (\Theta - \Theta_{\text{th}}) \left( 1 + \frac{C_M}{\mu} [\Theta - \Theta_{\text{th}}] \right), \quad (11)$$

493 where  $\kappa = 0.4$  is the von Kármán constant,  $C_M \simeq 1.7$  a constant and  $\mu \simeq 0.6$  is  
494 a friction coefficient, taken to be the avalanche slope of the granular material.  
495 The fit of this law to the experimental data of Creyssels et al. (2009) and Ho  
496 et al. (2011) gives  $\Theta_{\text{th}} = 0.0035$ . The fit of Eq. 10 on these same data similarly  
497 gives  $\Omega \simeq 8$  and  $\Theta_{\text{th}} = 0.005$ . The sand flux angular distributions and the  
498 dune orientations in Fig. 9 are calculated using this law (11). We have checked  
499 that using the ordinary linear relationship (10) instead does not change the  
500 predicted dune orientations by more than a few degrees.

501 *Dune orientations* — Dune orientations are predicted with the dimensional  
 502 model of Courrech du Pont et al. (2014), from the sand flux time series com-  
 503 puted with the above transport law. Two orientations are possible depending  
 504 on the mechanism dominating the dune growth: elongation or bed instabil-  
 505 ity. The orientation  $\alpha$  corresponding the bed instability is then the one that  
 506 maximises the following growth rate (Rubin and Hunter 1987):

$$\sigma \propto \frac{1}{H_d W_d T} \int_0^T q_{\text{crest}} |\sin(\theta - \alpha)| dt, \quad (12)$$

507 where  $\theta$  is the wind orientation measured with respect to the same reference  
 508 as  $\alpha$ , and  $H_d$  and  $W_d$  are dimensional constants respectively representing the  
 509 dune height and width. The integral runs over a time  $T$ , which must be repre-  
 510 sentative of the characteristic period of the wind regime. The flux at the crest  
 511 is expressed as:

$$q_{\text{crest}} = q_{\text{sat}} [1 + \gamma |\sin(\theta - \alpha)|], \quad (13)$$

512 where the flux-up ratio  $\gamma$  has been calibrated to 1.6 using field studies, under-  
 513 water laboratory experiments and numerical simulations. Predictions of the  
 514 linear analysis of Gadal et al. (2019) and Delorme et al. (2020) give similar  
 515 results.

516 Similarly, the dune orientation corresponding to the elongation mechanism  
 517 is the one that verifies:

$$\tan(\alpha) = \frac{\langle q_{\text{crest}}(\alpha) \mathbf{e}_\theta \rangle \cdot \mathbf{e}_{WE}}{\langle q_{\text{crest}}(\alpha) \mathbf{e}_\theta \rangle \cdot \mathbf{e}_{SN}}, \quad (14)$$

518 where  $\langle \cdot \rangle$  denotes a vectorial time average. The unitary vectors  $\mathbf{e}_{WE}$ ,  $\mathbf{e}_{SN}$  and  
 519  $\mathbf{e}_\theta$  are in the West-East, South-North and wind directions, respectively.

520 The resulting computed dune orientations, blue and red arrows in Fig. 9,  
 521 then depend on a certain number of parameters (grain properties, flux-up ratio,  
 522 etc.), for which we take typical values for aeolian sandy deserts. Due to the lack  
 523 of measurements in the studied places, some uncertainties can be expected. We  
 524 therefore run a sensitivity test by calculating the dune orientations for grain  
 525 diameters ranging from 100  $\mu\text{m}$  to 400  $\mu\text{m}$  and for a speed-up ratio between  
 526 0.1 and 10 (wedges in Fig. 9).

---

**527 References**

- 528 Andreotti B (2004) A two-species model of aeolian sand transport. *J Fluid  
529 Mech* 510:47–70
- 530 Andreotti B, Claudin P, Douady S (2002) Selection of dune shapes and veloc-  
531 ities part 1: Dynamics of sand, wind and barchans. *The European Physical  
532 Journal B-Condensed Matter and Complex Systems* 28(3):321–339
- 533 Andreotti B, Fourrière A, Ould-Kaddour F, Murray B, Claudin P (2009) Gi-  
534 ant aeolian dune size determined by the average depth of the atmospheric  
535 boundary layer. *Nature* 457:1120–1123
- 536 Andreotti B, Claudin P, Devauchelle O, Durán O, Fourrière A (2012) Bedforms  
537 in a turbulent stream: ripples, chevrons and antidunes. *J Fluid Mech* 690:94–  
538 128
- 539 Ashkenazy Y, Yizhaq H, Tsoar H (2012) Sand dune mobility under climate  
540 change in the kalahari and australian deserts. *Climatic Change* 112:901–923
- 541 Baddock M, Livingstone I, Wiggs G (2007) The geomorphological significance  
542 of airflow patterns in transverse dune interdunes. *Geomorphology* 87:322–  
543 336
- 544 Bagnold RA (1941) *The Physics of Blown Sand and Desert Dunes*. London :  
545 Methuen : Chapman & Hall
- 546 Baines PG (1995) Topographic effects in stratified flows. Cambridge university  
547 press
- 548 Bauer BO, Sherman DJ, Wolcott JF (1992) Sources of uncertainty in shear  
549 stress and roughness length estimates derived from velocity profiles. *The  
550 Professional Geographer* 44:453–464
- 551 Belcher S, JCR H (1998) Turbulent flow over hills and waves. *Annu Rev Fluid  
552 Mech* 30:507–538
- 553 Blumberg DG, Greeley R (1996) A comparison of general circulation model  
554 predictions to sand drift and dune orientations. *J Clim* 9:3248–3259
- 555 Bristow NR, Best J, Wiggs GFS, Nield JM, Baddock MC, Delorme P, Chris-  
556 tensen KT (2022) Topographic perturbation of turbulent boundary layers  
557 by low-angle, early-stage aeolian dunes. *Earth Surf Process Landf* n/a(n/a),  
558 DOI <https://doi.org/10.1002/esp.5326>
- 559 Brookfield M (1977) The origin of bounding surfaces in ancient aeolian sand-  
560 stones. *Sedimentology* 24(3):303–332
- 561 Brown S, Nickling WG, Gillies JA (2008) A wind tunnel examination of shear  
562 stress partitioning for an assortment of surface roughness distributions. *J  
563 Geophys Res* 113:F02S06
- 564 Chang H, Simons D (1970) The bed configuration of straight sand-bed channels  
565 when flow is nearly critical. *J Fluid Mech* 42(3):491–495
- 566 Charru F, Andreotti B, Claudin P (2013) Sand ripples and dunes. *Annu Rev  
567 Fluid Mech* 45:469–493
- 568 Claudin P, Wiggs G, Andreotti B (2013) Field evidence for the upwind velocity  
569 shift at the crest of low dunes. *Boundary-Layer Meteorol* 148:195–206
- 570 Claudin P, Durán O, Andreotti B (2017) Dissolution instability and roughen-  
571 ing transition. *J Fluid Mech* 832:R2

- 572 Claudin P, Louge M, Andreotti B (2021) Basal pressure variations induced by  
573 a turbulent flow over a wavy surface. *Frontiers in Physics* 9:682564
- 574 Colombini M (2004) Revisiting the linear theory of sand dune formation. *J  
575 Fluid Mech* 502:1–16
- 576 Courrech du Pont S (2015) Dune morphodynamics. *C R Phys* 16:118–138
- 577 Courrech du Pont S, Narteau C, Gao X (2014) Two modes for dune orientation.  
578 *Geology* 42:743–746
- 579 Creyssels M, Dupont P, El Moctar AO, Valance A, Cantat I, Jenkins JT, Pasini  
580 JM, Rasmussen KR (2009) Saltating particles in a turbulent boundary layer:  
581 experiment and theory. *J Fluid Mech* 625:47–74
- 582 de Winter W, Donker J, Sterk G, Van Beem J, Ruessink G (2020) Regional  
583 versus local wind speed and direction at a narrow beach with a high and  
584 steep foredune. *Plos one* 15(1):e0226983
- 585 Dee DP, Uppala SM, Simmons AJ, Berrisford P, Poli P, Kobayashi S, Andrae  
586 U, Balmaseda M, Balsamo G, Bauer dP, et al. (2011) The era-interim re-  
587 analysis: Configuration and performance of the data assimilation system. *Q  
588 J R Meteorol Soc* 137:553–597
- 589 Delorme P, Wiggs G, Baddock M, Claudin P, Nield J, Valdez A (2020) Dune  
590 initiation in a bimodal wind regime. *J Geophys Res* 125:e2020JF005757
- 591 Durán O, Claudin P, Andreotti B (2011) On aeolian transport: Grain-scale  
592 interactions, dynamical mechanisms and scaling laws. *Aeolian Res* 3:243–  
593 270
- 594 Durran DR (1990) Mountain waves and downslope winds. In: *Atmospheric  
595 processes over complex terrain*, Springer, pp 59–81
- 596 Dyer A (1974) A review of flux-profile relationships. *Boundary-Layer Meteorol  
597* 7(3):363–372
- 598 Ewing RC, Kocurek G, Lake LW (2006) Pattern analysis of dune-field param-  
599 eters. *Earth Surf Process Landf* 31(9):1176–1191
- 600 Farr TG, Rosen PA, Caro E, Crippen R, Duren R, Hensley S, Kobrick M,  
601 Paller M, Rodriguez E, Roth L, et al. (2007) The shuttle radar topography  
602 mission. *Rev Geophys* 45
- 603 Fernando H, Mann J, Palma J, Lundquist JK, Barthelmie RJ, Belo-Pereira M,  
604 Brown W, Chow F, Gerz T, Hocut C, et al. (2019) The perdigão: Peering  
605 into microscale details of mountain winds. *Bull Am Meteorol Soc* 100:799–  
606 819
- 607 Field JP, Pelletier JD (2018) Controls on the aerodynamic roughness length  
608 and the grain-size dependence of aeolian sediment transport. *Earth Surf  
609 Process Landf* 43:2616–2626
- 610 Finnigan J, Raupach M, Bradley E, Aldis G (1990) A wind tunnel study  
611 of turbulent flow over a two-dimensional ridge. *Boundary-Layer Meteorol  
612* 50:277–317
- 613 Finnigan J, Ayotte K, Harman I, Katul G, Oldroyd H, Patton E, Poggi D,  
614 Ross A, Taylor P (2020) Boundary-layer flow over complex topography.  
615 *Boundary-Layer Meteorol* 177:247–313
- 616 Flack K, Schultz M (2010) Review of hydraulic roughness scales in the fully  
617 rough regime. *Journal of Fluids Engineering* 132:041203

- 618 Fourrière A, Claudin P, Andreotti B (2010) Bedforms in a turbulent stream:  
619 formation of ripples by primary linear instability and of dunes by nonlinear  
620 pattern coarsening. *J Fluid Mech* 649:287–328
- 621 Frederick KA, Hanratty TJ (1988) Velocity measurements for a turbulent non-  
622 separated flow over solid waves. *Exp Fluids* 6:477–486
- 623 Fryberger SG, Dean G (1979) Dune forms and wind regime. A study of global  
624 sand seas 1052:137–169
- 625 Gadal C, Narteau C, Courrech Du Pont S, Rozier O, Claudin P (2019) Incip-  
626 ient bedforms in a bidirectional wind regime. *J Fluid Mech* 862:490–516
- 627 Gadal C, Narteau C, Courrech du Pont S, Rozier O, Claudin P (2020) Peri-  
628 odicity in fields of elongating dunes. *Geology* 48:343–347
- 629 Gadal C, Delorme P, Narteau C, Wiggs G, Baddock M, Nield JM, Claudin  
630 P (2022) Data used in 'Local wind regime induced by giant linear dunes:  
631 comparison of ERA5-Land re-analysis with surface measurements'. DOI  
632 10.5281/zenodo.6343138
- 633 Garratt JR (1994) The atmospheric boundary layer. *Earth-Science Reviews*  
634 37(1-2):89–134
- 635 Garvey B, Castro IP, Wiggs G, Bullard J (2005) Measurements of flows over  
636 isolated valleys. *Boundary-Layer Meteorol* 117(3):417–446
- 637 Gong W, Ibbetson A (1989) A wind tunnel study of turbulent flow over model  
638 hills. *Boundary-Layer Meteorol* 49:113–148
- 639 Gong W, Taylor P, Dörnbrack A (1996) Turbulent boundary-layer flow over  
640 fixed aerodynamically rough two-dimensional sinusoidal waves. *J Fluid Mech*  
641 312:1–37
- 642 Guérin A, Derr J, Du Pont SC, Berhanu M (2020) Streamwise dissolution  
643 patterns created by a flowing water film. *Phys Rev Lett* 125(19):194502
- 644 Gunn A, Casasanta G, Di Liberto L, Falcini F, Lancaster N,  
645 Jerolmack DJ (2021a) What sets aeolian dune height? DOI  
646 <https://doi.org/10.31223/X5QG8S>
- 647 Gunn A, Wanker M, Lancaster N, Edmonds D, Ewing R, Jerolmack  
648 D (2021b) Circadian rhythm of dune-field activity. *Geophys Res Lett*  
649 48:e2020GL090924
- 650 Harris CR, Millman KJ, van der Walt SJ, Gommers R, Virtanen P, Cournapeau D,  
651 Wieser E, Taylor J, Berg S, Smith NJ, et al. (2020) Array program-  
652 ming with numpy. *Nature* 585:357–362
- 653 Havholm KG, Kocurek G (1988) A preliminary study of the dynamics of  
654 a modern draa, algodones, southeastern california, usa. *Sedimentology*  
655 35(4):649–669
- 656 Hersbach H, Bell B, Berrisford P, Hirahara S, Horányi A, Muñoz-Sabater J,  
657 Nicolas J, Peubey C, Radu R, Schepers D, et al. (2020) The era5 global  
658 reanalysis. *Q J R Meteorol Soc* 146:1999–2049
- 659 Hesp P, Illenberger W, Rust I, McLachlan A, Hyde R (1989) Some aspects of  
660 transgressive dunefield and transverse dune geomorphology and dynamics,  
661 south coast, south africa. *Zeitschrift fur Geomorphologie*, Supplementband  
662 73:111–123

- 663 Hesp PA, Hastings K (1998) Width, height and slope relationships and aero-  
664 dynamic maintenance of barchans. *Geomorphology* 22(2):193–204
- 665 Hesp PA, Smyth TAG, Nielsen P, Walker IJ, Bauer BO, Davidson-Arnott R  
(2015) Flow deflection over a foredune. *Geomorphology* 230:64–74
- 666 Ho TD, Valance A, Dupont P, Ould El Moctar A, Tuan Duc H, Valance A,  
667 Dupont P, Ould El Moctar A (2011) Scaling laws in aeolian sand transport.  
668 *Phys Rev Lett* 106:4–7
- 669 Hood DR, Ewing RC, Roback KP, Runyon K, Avouac JP, McEnroe M (2021)  
670 Inferring airflow across martian dunes from ripple patterns and dynamics.  
671 *Frontiers in Earth Science* 9:702828
- 672 Howard AD (1977) Effect of slope on the threshold of motion and its applica-  
673 tion to orientation of wind ripples. *Geological Society of America Bulletin*  
674 88:853–856
- 675 Hu Z, Gao X, Lei J, Zhou N (2021) Geomorphology of aeolian dunes in the  
676 western sahara desert. *Geomorphology* 392:107916
- 677 Hunt J, Leibovich S, Richards K (1988) Turbulent shear flows over low hills.  
678 *Q J R Meteorol Soc* 114:1435–1470
- 679 Hunt JCR, Vilenski GG, Johnson ER (2006) Stratified separated flow around  
680 a mountain with an inversion layer below the mountain top. *J Fluid Mech*  
681 556:105–119
- 682 Hunter JD (2007) Matplotlib: A 2d graphics environment. *Computing in sci-  
683 ence & engineering* 9:90–95
- 684 Iversen JD, Rasmussen KR (1999) The effect of wind speed and bed slope on  
685 sand transport. *Sedimentology* 46:723–731
- 686 Jackson PS, Hunt JCR (1975) Turbulent wind flow over a low hill. *Q J R  
687 Meteorol Soc* 101:929–955
- 688 Jiang Q (2014) Applicability of reduced-gravity shallow-water theory to atmo-  
689 pheric flow over topography. *J Atmos Sci* 71:1460–1479
- 690 Jolivet M, Braucher R, Dovchintseren D, Hocquet S, Schmitt J, ASTER Team  
691 (2021) Erosion around a large-scale topographic high in a semi-arid sedimen-  
692 tary basin: Interactions between fluvial erosion, aeolian erosion and aeolian  
693 transport. *Geomorphology* 386:107747
- 694 Kennedy JF (1963) The mechanics of dunes and antidunes in erodible-bed  
695 channels. *J Fluid Mech* 16(4):521–544
- 696 Kim HG, Patel VC, Lee CM (2000) Numerical simulation of wind flow over  
697 hilly terrain. *J Wind Eng Ind Aerodyn* 87:45–60
- 698 Lancaster J, Lancaster N, Seely M (1984) Climate of the central namib desert.  
699 *Madoqua* 1984:5–61
- 700 Lancaster N (1985) Winds and sand movements in the namib sand sea. *Earth  
701 Surf Process Landf* 10:607–619
- 702 Lancaster N, Nickling W, Neuman CM, Wyatt V (1996) Sediment flux and  
703 airflow on the stoss slope of a barchan dune. *Geomorphology* 17(1-3):55–62
- 704 Lewis HW, Mobbs SD, Lehning M (2008) Observations of cross-ridge flows  
705 across steep terrain. *Q J R Meteorol Soc* 134:801–816
- 706 Liu ZYC, Zimbelman JR (2015) Recent near-surface wind directions inferred  
707 from mapping sand ripples on martian dunes. *Icarus* 261:169–181

- 709 Livingstone I, Warren A (2019) Aeolian geomorphology: a new introduction.  
710 Wiley
- 711 Livingstone I, Bristow C, Bryant RG, Bullard J, White K, Wiggs GFS, Baas  
712 ACW, Bateman MD, Thomas DSG (2010) The namib sand sea digital  
713 database of aeolian dunes and key forcing variables. *Aeolian Res* 2:93–104
- 714 Lorenz R, Claudin P, Andreotti B, Radebaugh J, Tokano T (2010) A 3 km  
715 atmospheric boundary layer on titan indicated by dune spacing and huygens  
716 data. *Icarus* 205:719–721
- 717 Lü P, Narteau C, Dong Z, Rozier O, Du Pont SC (2017) Unravelling raked  
718 linear dunes to explain the coexistence of bedforms in complex dunefields.  
719 *Nature communications* 8:1–9
- 720 Lü P, Narteau C, Dong Z, Claudin P, Rodriguez S, An Z, Fernandez-Cascales  
721 L, Gadal C, Courrech du Pont S (2021) Direct validation of dune instability  
722 theory. *Proceedings of the National Academy of Sciences* 118
- 723 Mason P, Sykes R (1979) Flow over an isolated hill of moderate slope. *Q J R  
724 Meteorol Soc* 105:383–395
- 725 Mckenna Neuman C, Lancaster N, Nickling WG (1997) Relations between  
726 dune morphology, air flow, and sediment flux on reversing dunes, Sil-  
727 ver Peak, Nevada. *Sedimentology* 44(6):1103–1111, DOI 10.1046/j.1365-  
728 3091.1997.d01-61.x
- 729 Mizumura K (1995) Free-surface profile of open-channel flow with wavy bound-  
730 ary. *J Hydraul Eng* 121(7):533–539
- 731 Monin AS, Obukhov AM (1954) Basic laws of turbulent mixing in the surface  
732 layer of the atmosphere. *Contrib Geophys Inst Acad Sci USSR* 151(163):e187
- 733 Mulligan KR (1988) Velocity profiles measured on the windward slope of a  
734 transverse dune. *Earth Surf Process Landf* 13(7):573–582
- 735 Muñoz-Sabater J, Dutra E, Agustí-Panareda A, Albergel C, Arduini G, Bal-  
736 samo G, Boussetta S, Choulga M, Harrigan S, Hersbach H, et al. (2021)  
737 Era5-land: A state-of-the-art global reanalysis dataset for land applications.  
738 *Earth Syst Sci Data* 13:4349–4383
- 739 Nield JM, King J, Wiggs GFS, Leyland J, Bryant RG, Chiverrell RC, Darby  
740 SE, Eckhardt FD, Thomas DSG, Vircavs LH, Washington R (2014) Esti-  
741 mating aerodynamic roughness over complex surface terrain. *J Geophys Res*  
742 118:12948–12961
- 743 Nield JM, Wiggs GF, Baddock MC, Hipondoka MH (2017) Coupling leeside  
744 rainfall to avalanche characteristics in aeolian dune dynamics. *Geology*  
745 45(3):271–274
- 746 Pähzt T, Durán O (2020) Unification of aeolian and fluvial sediment transport  
747 rate from granular physics. *Phys Rev Lett* 124:168001
- 748 Pearce KI, Walker IJ (2005) Frequency and magnitude biases in the 'Fryberger'  
749 model, with implications for characterizing geomorphically effective winds.  
750 *Geomorphology* 68:39–55
- 751 Pelletier JD, Field JP (2016) Predicting the roughness length of turbulent flows  
752 over landscapes with multi-scale microtopography. *Earth Surface Dynamics*  
753 4:391–405

- 754 Poggi D, Katul G, Albertson J, Ridolfi L (2007) An experimental investigation  
755 of turbulent flows over a hilly surface. *Phys Fluids* 19:036601
- 756 Rasmussen KR (1989) Some aspects of flow over coastal dunes. *Proceedings of*  
757 *the Royal Society of Edinburgh, Section B: Biological Sciences* 96:129–147
- 758 Rasmussen KR, Iversen JD, Rautaheimo P (1996) Saltation and wind flow  
759 interaction in a variable slope wind tunnel. *Geomorphology* 17:19–28
- 760 Raupach M (1992) Drag and drag partition on rough surfaces. *Boundary-Layer*  
761 *Meteorol* 60:375–395
- 762 Rubin DM, Hunter RE (1987) Bedform alignment in directionally varying  
763 flows. *Science* 237:276–278
- 764 Runyon K, Bridges N, Ayoub F, Newman C, Quade J (2017) An integrated  
765 model for dune morphology and sand fluxes on mars. *Earth and Planetary*  
766 *Science Letters* 457:204–212
- 767 Sauermann G, Andrade Jr J, Maia L, Costa U, Araújo A, Herrmann H (2003)  
768 Wind velocity and sand transport on a barchan dune. *Geomorphology* 54(3–  
769 4):245–255
- 770 Seidel DJ, Zhang Y, Beljaars A, Golaz JC, Jacobson AR, Medeiros B (2012)  
771 Climatology of the planetary boundary layer over the continental united  
772 states and europe. *J Geophys Res* 117:D17106
- 773 Shao Y (2008) Physics and modelling of wind erosion, vol 37. Springer Science  
774 & Business Media
- 775 Shen Y, Zhang C, Huang X, Wang X, Cen S (2019) The effect of wind speed  
776 averaging time on sand transport estimates. *Catena* 175:286–293
- 777 Sheridan PF, Vosper SB (2006) A flow regime diagram for forecasting lee  
778 waves, rotors and downslope winds. *Meteorol Appl* 13:179–195
- 779 Sherman CA (1978) A mass-consistent model for wind fields over complex  
780 terrain. *J Appl Meteorol Clim* 17(3):312–319
- 781 Sherman D, Farrell E (2008) Aerodynamic roughness lengths over movable  
782 beds: Comparison of wind tunnel and field data. *J Geophys Res* 113:1–10
- 783 Sherman DJ, Li B (2012) Predicting aeolian sand transport rates: A reevalu-  
784 ation of models. *Aeolian Res* 3:371–378
- 785 Smith AB, Jackson DWT, Cooper JAG (2017) Three-dimensional airflow and  
786 sediment transport patterns over barchan dunes. *Geomorphology* 278:28–42
- 787 Song Q, Gao X, Lei J, Li S (2019) Spatial distribution of sand dunes and their  
788 relationship with fluvial systems on the southern margin of the taklimakan  
789 desert, china. *Geomatics, Natural Hazards and Risk* 10:2408–2428
- 790 Spalding DB (1961) A single formula for the law of the wall. *Journal of Applied*  
791 *Mechanics* 28:455–458
- 792 Stull R (2006) 9 - the atmospheric boundary layer. In: Wallace JM, Hobbs PV  
793 (eds) *Atmospheric Science* (Second Edition), second edition edn, Academic  
794 Press, San Diego, pp 375–417
- 795 Stull RB (1988) An introduction to boundary layer meteorology, vol 13.  
796 Springer Science & Business Media
- 797 Sullivan PP, McWilliams JC (2010) Dynamics of winds and currents coupled  
798 to surface waves. *Annu Rev Fluid Mech* 42:19–42

- 799 Sweet M, Kocurek G (1990) An empirical model of aeolian dune lee-face air-  
800 flow. *Sedimentology* 37(6):1023–1038
- 801 Sykes RI (1980) An asymptotic theory of incompressible turbulent boundary-  
802 layer flow over a small hump. *J Fluid Mech* 101:647–670
- 803 Taylor P, Teunissen H (1987) The Askervein hill project: overview and back-  
804 ground data. *Boundary-Layer Meteorol* 39:15–39
- 805 Taylor P, Mason P, Bradley E (1987) Boundary-layer flow over low hills.  
806 *Boundary-Layer Meteorol* 39:107–132
- 807 Tsoar H, Yaalon DH (1983) Deflection of sand movement on a sinuous longi-  
808 tudinal (seif) dune: use of fluorescent dye as tracer. *Sedimentary Geology*  
809 36(1):25–39
- 810 Ungar JE, Haff PK (1987) Steady state saltation in air. *Sedimentology* 34:289–  
811 299
- 812 Unsworth C, Parsons D, Hardy R, Reesink A, Best J, Ashworth P, Keevil G  
813 (2018) The impact of nonequilibrium flow on the structure of turbulence  
814 over river dunes. *Water Resour Res* 54:6566–6584
- 815 Uppala SM, Källberg P, Simmons AJ, Andrae U, Bechtold VDC, Fiorino M,  
816 Gibson J, Haseler J, Hernandez A, Kelly G, et al. (2005) The era-40 re-  
817 analysis. *Q J R Meteorol Soc* 131:2961–3012
- 818 Valance A, Rasmussen K, Ould El Moctar A, Dupont P (2015) The physics  
819 of aeolian sand transport. *C R Phys* 16:1–13
- 820 Venditti JG, Best JL, Church M, Hardy RJ (2013) Coherent Flow Structures  
821 at Earth’s Surface. John Wiley & Sons
- 822 Virtanen P, Gommers R, Oliphant TE, Haberland M, Reddy T, Cournapeau  
823 D, Burovski E, Peterson P, Weckesser W, Bright J, et al. (2020) Scipy 1.0:  
824 fundamental algorithms for scientific computing in python. *Nature methods*  
825 17:261–272
- 826 Vogelezang D, Holtslag A (1996) Evaluation and model impacts of alternative  
827 boundary-layer height formulations. *Boundary-Layer Meteorol* 81:245–269
- 828 Vosper SB (2004) Inversion effects on mountain lee waves. *Q J R Meteorol Soc*  
829 130:1723–1748
- 830 Walker I, Davidson-Arnott R, Bauer B, Hesp P, Delgado-Fernandez I, Oller-  
831 head J, Smyth T (2017) Scale-dependent perspectives on the geomorphology  
832 and evolution of beach-dune systems. *Earth-Science Review* 171:220–253
- 833 Walker IJ, Nickling WG (2002) Dynamics of secondary airflow and sediment  
834 transport over and in the lee of transverse dunes. *Prog Phys Geogr* 26(1):47–  
835 75
- 836 Walker IJ, Hesp PA, Davidson-Arnott RG, Ollerhead J (2006) Topographic  
837 steering of alongshore airflow over a vegetated foredune: Greenwich dunes,  
838 prince edward island, canada. *Journal of Coastal Research* 22(5):1278–1291
- 839 Walker IJ, Hesp PA, Davidson-Arnott RG, Bauer BO, Namikas SL, Ollerhead  
840 J (2009) Responses of three-dimensional flow to variations in the angle of  
841 incident wind and profile form of dunes: Greenwich dunes, prince edward  
842 island, canada. *Geomorphology* 105:127–138
- 843 Walmsley JL, Salmon J, Taylor P (1982) On the application of a model of  
844 boundary-layer flow over low hills to real terrain. *Boundary-Layer Meteorol*

- 845 23(1):17–46
- 846 Weaver C, Wiggs G (2011) Field measurements of mean and turbulent airflow  
847 over a barchan sand dune. *Geomorphology* 128:32–41
- 848 Wiggs G, Bullard J, Garvey B, Castro I (2002) Interactions between airflow  
849 and valley topography with implications for aeolian sediment transport.  
850 *Physical Geography* 23:366–380
- 851 Wood N (2000) Wind flow over complex terrain: a historical perspective and  
852 the prospect for large-eddy modelling. *Boundary-Layer Meteorol* 96(1):11–  
853 32
- 854 Zhang C, Li Q, Zhou N, Zhang J, Kang L, Shen Y, Jia W (2016) Field obser-  
855 vations of wind profiles and sand fluxes above the windward slope of a sand  
856 dune before and after the establishment of semi-buried straw checkerboard  
857 barriers. *Aeolian Res* 20:59–70
- 858 Zilker DP, Hanratty TJ (1979) Influence of the amplitude of a solid wavy wall  
859 on a turbulent flow. part 2. separated flows. *J Fluid Mech* 90:257–271
- 860 Zilker DP, Cook GW, Hanratty TJ (1977) Influence of the amplitude of a solid  
861 wavy wall on a turbulent flow. part 1. non-separated flows. *J Fluid Mech*  
862 82:29–51

---

863      **Local wind regime induced by giant linear dunes**  
 864      — Supplementary Material —

865    **C. Gadal\* · P. Delorme · C. Narteau · G.F.S. Wiggs · M. Baddock ·**  
 866    **J.M. Nield · P. Claudin**

867  
 868    \* Institut de Mécanique des Fluides de Toulouse, Université de Toulouse Paul  
 869    Sabatier, CNRS, Toulouse INP-ENSEEIHT, Toulouse, France.  
 870    [cyril.gadal@imft.fr](mailto:cyril.gadal@imft.fr)

871    **1. Shear velocity and calibration of the hydrodynamical roughness**

872    As the regionally predicted and locally measured velocities are available at  
 873    different heights, we can not compare them directly. We therefore convert  
 874    all velocities into shear velocities  $u_*$ , characteristic the turbulent logarithmic  
 875    velocity profile (Spalding 1961; Stull 1988):

$$\frac{u(z)}{u_*} = \frac{1}{\kappa} \ln \left( \frac{z}{z_0} \right), \quad (15)$$

876    where  $z$  is the vertical coordinate,  $\kappa = 0.4$  the von Kármán constant and  $z_0$  the  
 877    hydrodynamic roughness. Note that, strickly speaking, this logarithmic profile  
 878    is valid for a neutrally stratified ABL only. Vertical density gradients occurring  
 879    in other conditions may thus induce large discrepancies (Monin and Obukhov  
 880    1954; Garratt 1994; Dyer 1974). However, as our wind measurements are in  
 881    the flow region close enough to the surface, where these effects are negligible,  
 882    this logarithmic wind profile remains a fairly good approximation in all conditions  
 883    (Gunn et al. 2021b). Several measurements of hydrodynamic roughnesses  
 884    are available (Raupach 1992; Bauer et al. 1992; Brown et al. 2008; Nield et al.  
 885    2014). In the absence of sediment transport, it is governed by the geometric  
 886    features of the bed (Flack and Schultz 2010; Pelletier and Field 2016). When  
 887    aeolian saltation occurs, it is rather controlled by the altitude of Bagnold's  
 888    focal point (Durán et al. 2011; Valance et al. 2015), which depends on the  
 889    wind velocity and grain properties (Sherman and Farrell 2008; Zhang et al.  
 890    2016; Field and Pelletier 2018). Whether associated with geometric features  
 891    or with sediment transport, its typical order of magnitude is the millimetre  
 892    scale on sandy surfaces.

893    We do not have precise velocity vertical profiles to be able to deduce an  
 894    accurate value of  $z_0$  in the various environments of the meteorological stations  
 895    (vegetated, arid, sandy). Our approach is to rather select the hydrodynamic  
 896    roughness which allows for the best possible matching between the regionally  
 897    predicted and locally measured winds, i.e. minimising the relative difference  $\delta$   
 898    between the wind vectors of both datasets:

$$\delta = \frac{\sqrt{\langle \| \mathbf{u}_{*,\text{era}} - \mathbf{u}_{*,\text{station}} \|^2 \rangle}}{\sqrt{\langle \| \mathbf{u}_{*,\text{era}} \|^2 \rangle \langle \| \mathbf{u}_{*,\text{station}} \|^2 \rangle}}, \quad (16)$$

where  $\langle \cdot \rangle$  denotes time average. This parameter is computed for values of  $z_0$  in ERA5-Land analysis ranging from  $10^{-5}$  m to  $10^{-2}$  m for the four different stations. Note that for the North Sand Sea and South Sand Sea stations, where the giant dunes feedback presumably affect the wind, we take into account the non-deflected winds only in the calculation of  $\delta$  (with a  $15^\circ$  tolerance).

As shown in Online Resource Fig. S3, the minimum values of  $\delta$  in the space  $(z_0^{\text{ERA5Land}}, z_0^{\text{local}})$  form a line. We thus set the roughness in the ERA5-Land analysis to the typical value  $z_0 = 10^{-3}$  m, and deduce the corresponding ones for the local stations. It leads to 2.7, 0.8, 0.1 and 0.5 mm for the Etosha West, North Sand Sea, Huab and South Sand Sea stations, respectively. Importantly, this approach somewhat impacts the calculation of the shear velocities, but not that of the wind directions. As such, most of our conclusions are independent of such a choice. However, it may affect the magnitude of the wind velocity attenuation/amplification in flow confinement situations.

## 2. Computation of the ABL characteristics

The estimation of the non-dimensional numbers associated with the ABL requires the computation of representative meteorological quantities. In arid areas, the vertical structure of the atmosphere can be approximated by a well mixed convective boundary layer of height  $H$ , topped by the stratified free atmosphere (Stull 1988; Shao 2008). In this context, one usually introduces the virtual potential temperature  $T_{\text{vp}}$ , which is a constant  $T_0$  inside the boundary layer, and increases linearly in the FA (Online Resource Fig. S8a):

$$T_{\text{vp}}(z) = \begin{cases} T_0 & \text{for } z \leq H, \\ T_0 \left( 1 + \frac{\Delta T_{\text{vp}}}{T_0} + \frac{N^2}{g}(z - H) \right) & \text{for } z \geq H, \end{cases} \quad (17)$$

where  $\Delta T_{\text{vp}}$  is the temperature discontinuity at the capping layer and  $N = \sqrt{g\partial_z T_{\text{vp}}/T_0}$  is the Brunt-Väisälä frequency, characteristic of the stratification. Note that, under the usual Boussinesq approximation, temperature and air density variations are simply related by  $\delta T_{\text{vp}}/T_0 \simeq -\delta\rho/\rho_0$  (see Online Resource of Andreotti et al. (2009)), so that  $N$  can equivalently be defined from the density gradient as next to (1).

The ERA5 dataset provides vertical profiles of the geopotential  $\phi$ , the actual temperature  $T$  and the specific humidity  $\eta$  at given pressure levels  $P$ . The vertical coordinate is then calculated as:

$$z = \frac{\phi R_t}{g R_t - \phi}, \quad (18)$$

where  $R_t = 6371229$  m is the reference Earth radius and  $g = 9.81$  m s $^{-2}$  is the gravitational acceleration. One also computes the virtual potential temperature as:

$$T_{\text{vp}} = T \left[ 1 + \left( \frac{M_d}{M_w} - 1 \right) \eta \right] \left( \frac{P_0}{P} \right)^{R/C_p}, \quad (19)$$

where  $P_0 = 10^5$  Pa is the standard pressure,  $R = 8.31$  J/K is the ideal gas constant,  $C_p \simeq 29.1$  J/K is the air molar heat capacity, and  $M_w = 0.018$  kg/Mol and  $M_d = 0.029$  kg/Mol are the molecular masses of water and dry air respectively. The specific humidity is related to the vapour pressure  $p_w$  as

$$\eta = \frac{\frac{M_w}{M_d} p_w}{p - \left(1 - \frac{M_w}{M_d}\right) p_w}. \quad (20)$$

The ERA5 dataset also provides an estimate of the ABL depth  $H$ , based on the behaviour of the Richardson vertical profile. This dimensionless number is defined as the ratio of buoyancy and flow shear terms, and can be expressed as  $\text{Ri} = N^2 / (\partial_z u)^2$ . It vanishes in the lower well-mixed layer where  $T_{\text{vp}}$  is constant, and increases in the stratified FA. Following the method and calibration of Vogeletezang and Holtlag (1996); Seidel et al. (2012), the value  $\text{Ri}(z) \simeq 0.25$  has been shown to be a good empirical criterion to give  $z \simeq H$  within a precision varying from 50% for the shallower ABL (e.g. at night) to 20% for situations of stronger convection.

Examples of vertical profiles of the virtual potential temperature deduced from ERA5 are shown in Online Resource Fig. S8a. For each of them, an average temperature is computed below the ABL depth ( $z < H$ ), and a linear function is fitted above, allowing us to extract the temperature jump  $\Delta T_{\text{vp}}$ . Importantly, some profiles display a vertical structure that cannot be approximated by the simple form (17) used here (Online Resource Fig. S8b). In practice, we removed from the analysis all of those leading to the unphysical case  $\Delta T_{\text{vp}} < 0$ . We have noticed that these ‘ill-processed’ profiles dominantly occur in winter and are evenly spread across the hours of the day. Importantly, they represent  $\simeq 12\%$  of the data only (Online Resource Fig. S8c,d), and we are thus confident that this data treatment does not affect our conclusions.

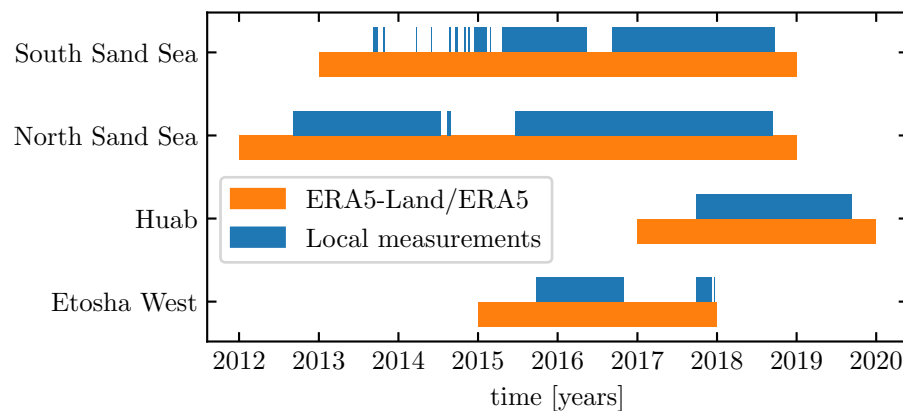


**Fig. S1** Gant chart representing the valid time steps for the two data sets, for all stations.

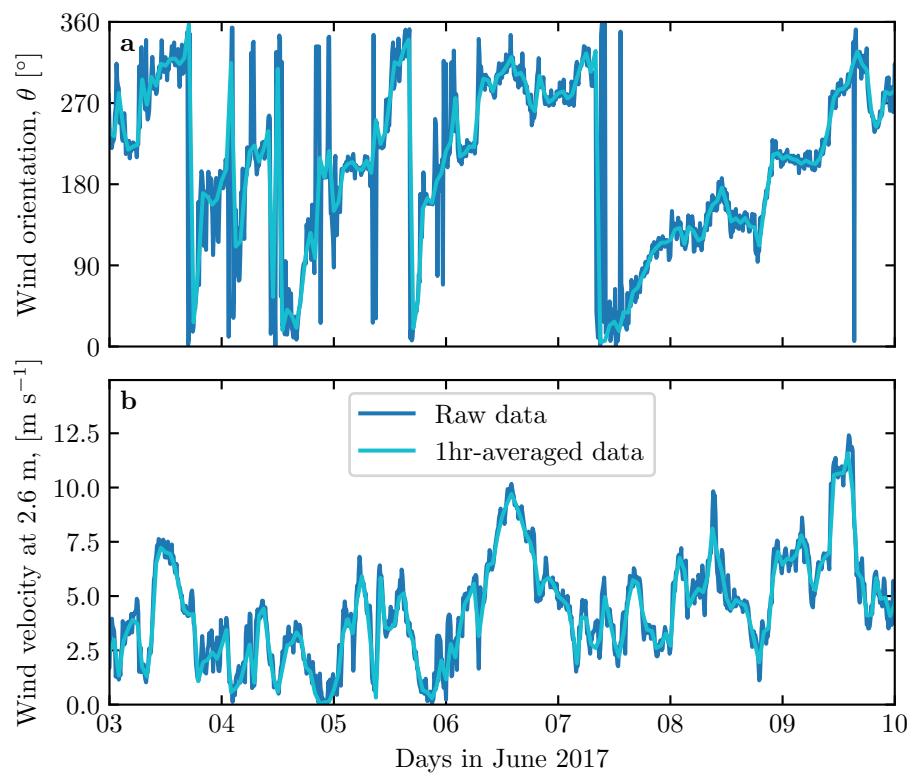


**Fig. S2** Comparison between raw local wind measurements, and hourly-averaged data for South Sand Sea station. **a:** wind direction. **b:** wind velocity at height 2.6 m.

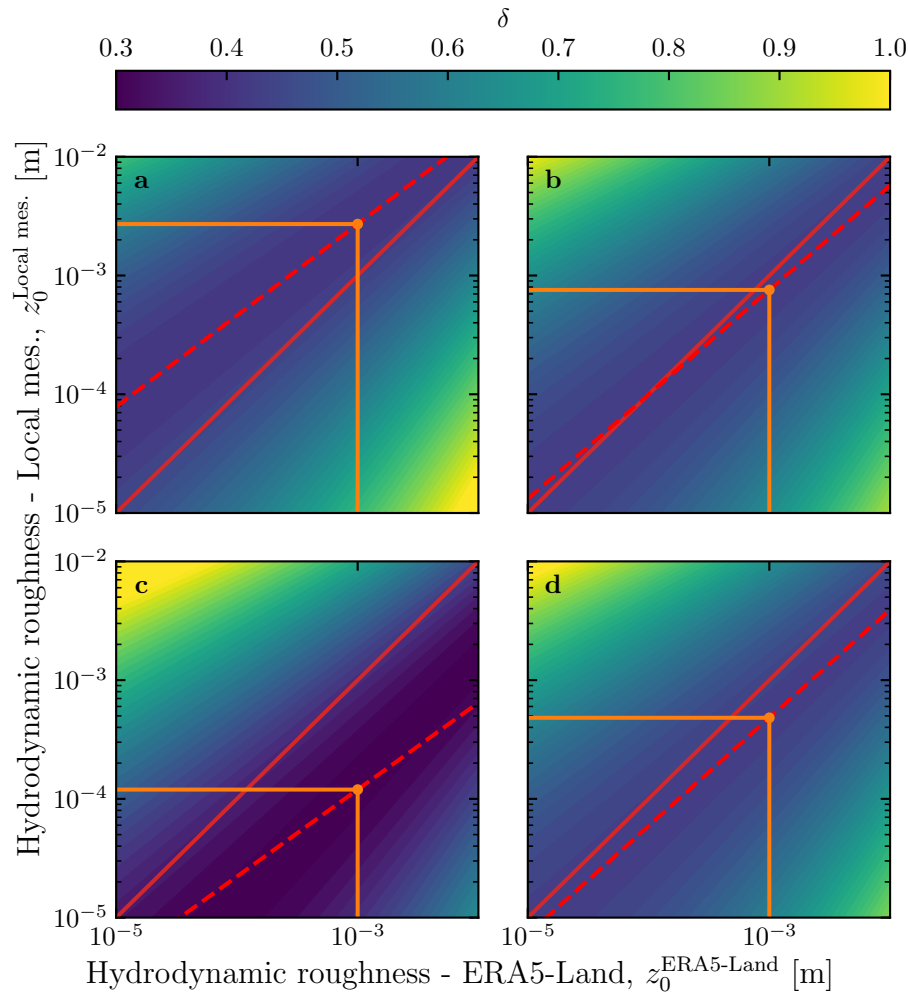


**Fig. S3** Calibration of hydrodynamic roughness. The parameter  $\delta$  (16) quantifying the difference between local and predicted winds is shown in colorscale as a function of the hydrodynamic roughnesses chosen for the ERA5-Land and for local winds, for the (a) Etosha West, (b) North Sand Sea, (c) Huab and (d) South Sand Sea stations. The red dashed and plain lines shows the minima of  $\delta$  and the identity line, respectively. The orange lines and dots highlight the chosen hydrodynamic roughnesses for the local winds deduced from setting  $z_0^{\text{ERA5Land}} = 1 \text{ mm}$ .

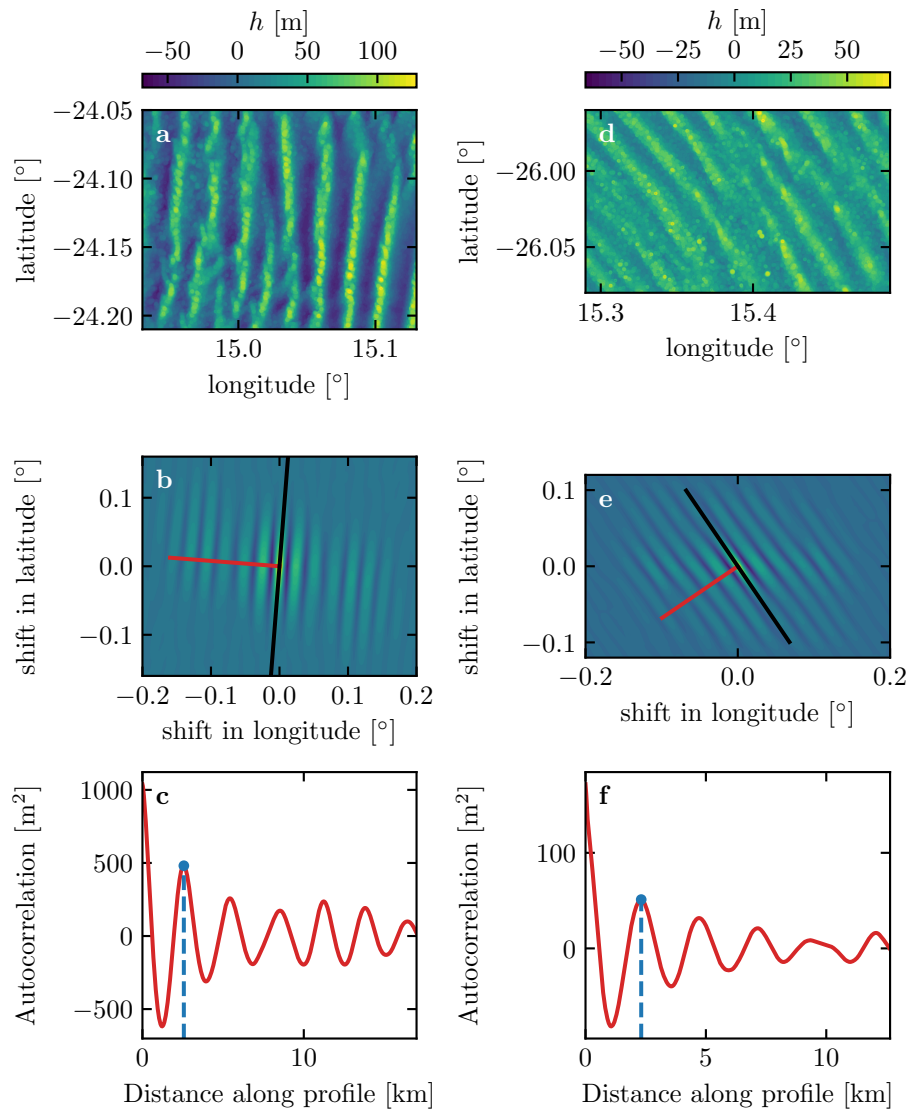


**Fig. S4** Analysis of the DEMs of the North Sand Sea (left column – panels **a**, **b**, **c**) and South Sand Sea (right column – panels **d**, **e**, **f**) stations. **a–d**: Bed elevation detrended by a fitted second order polynomial base-line. **b–e**: Autocorrelation matrix shown in colorscale. The black line shows the detected dune orientation, and the red line represents the autocorrelation profile along which the dune wavelength is calculated, displayed in **c–f**. The blue lines and dots show the first peak of the autocorrelation profile, whose abscissa gives the characteristic wavelength of the dune pattern.

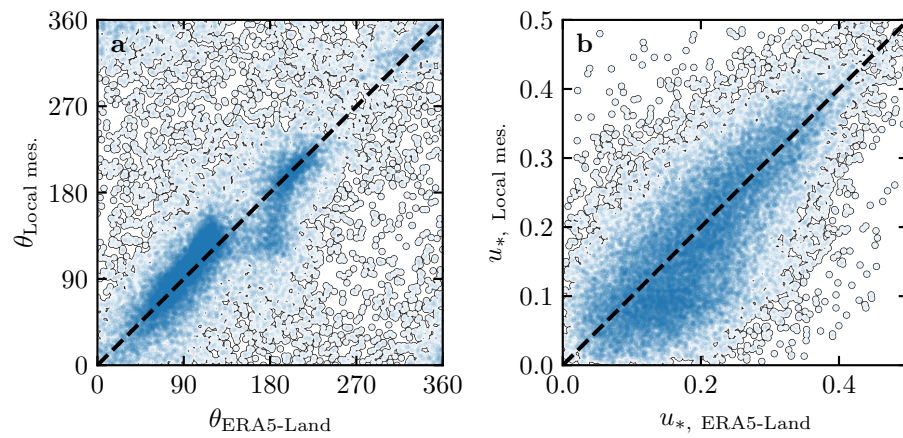


**Fig. S5** Statistical comparison of the wind orientation (a) and velocity (b) between the ERA5-Land dataset and the local measurements for the Huab and Etosha West stations. Data point clustering around identity lines (dashed and black) provide evidence for agreement of the two sets.

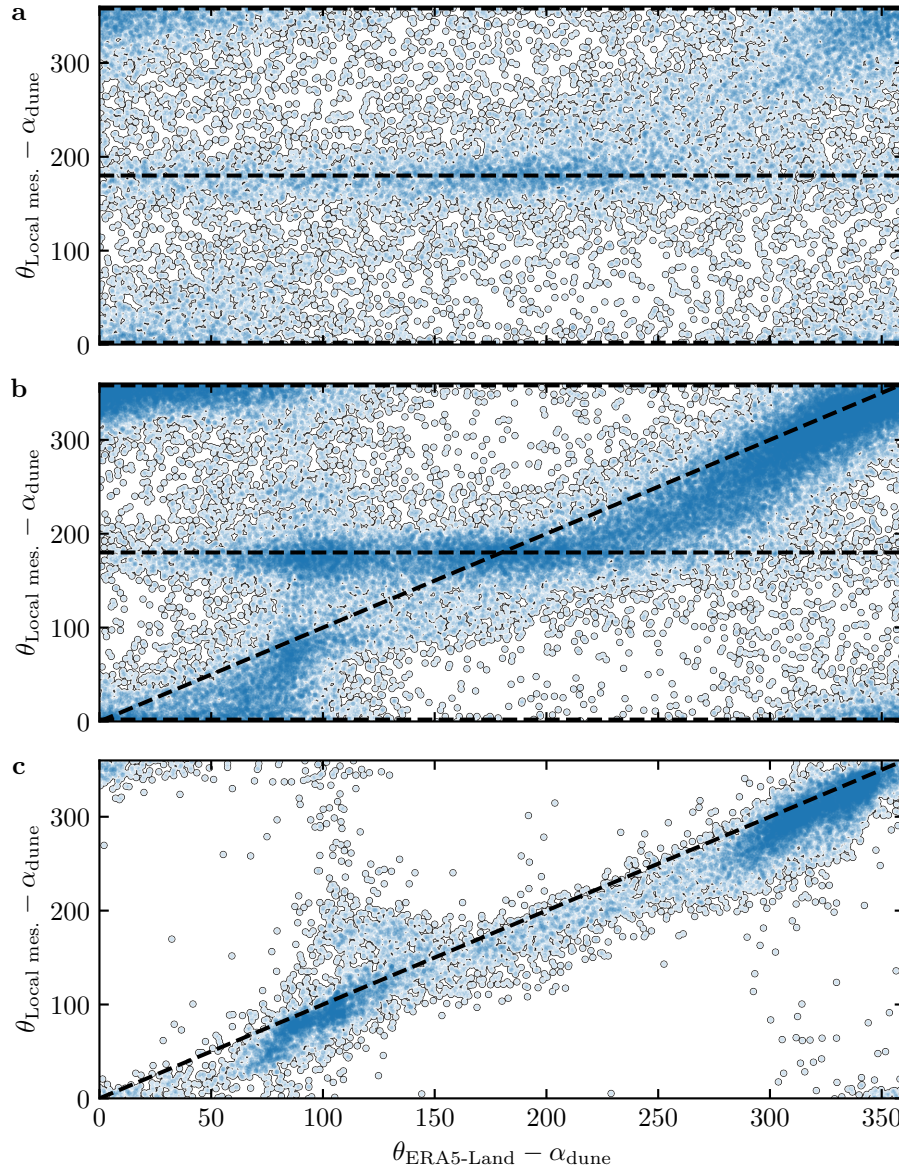


**Fig. S6** Statistical comparison of the wind orientation between the ERA5-Land dataset and the local measurements for the South Sand Sea and North Sand Sea stations, for different velocity ranges. **a:**  $u_{*,\text{ERA}} < 0.1 \text{ m s}^{-1}$ . **b:**  $0.1 < u_{*,\text{ERA}} \leq 0.25 \text{ m s}^{-1}$ . **c:**  $u_{*,\text{ERA}} \geq 0.25 \text{ m s}^{-1}$ . The measured dune orientations are subtracted to the wind orientation, which allows us to plot both stations on the same graph. Black dashed lines indicate locally measured orientations aligned with the dune crests (here 0°, 180° and 360° – panels a, b), as well as the identity lines (panels b, c).

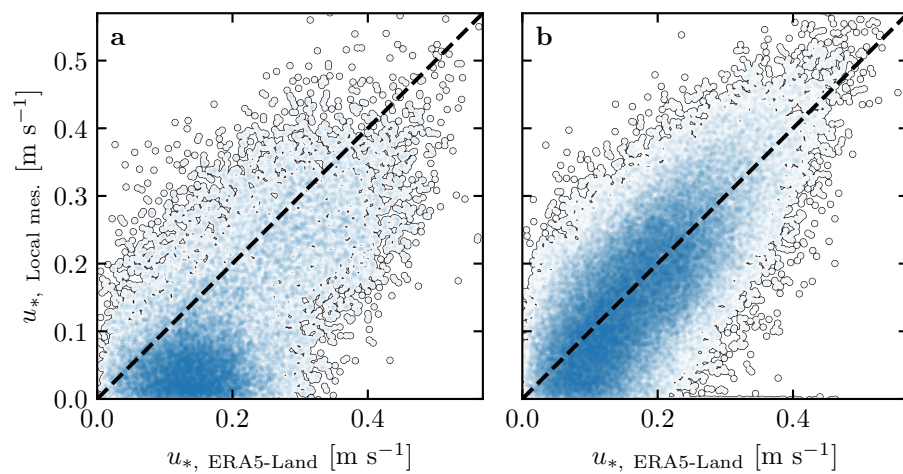


**Fig. S7** Statistical comparison of the wind velocity between the ERA5-Land dataset and the local measurements for the South Sand Sea and North Sand Sea stations. **a:** Nocturnal summer easterly wind. **b:** Diurnal southerly wind. Black dashed lines are identity lines. The angle ranges used to select diurnal and nocturnal summer winds are the same as those in Figs. 4 and Figs. 6 of the main article.

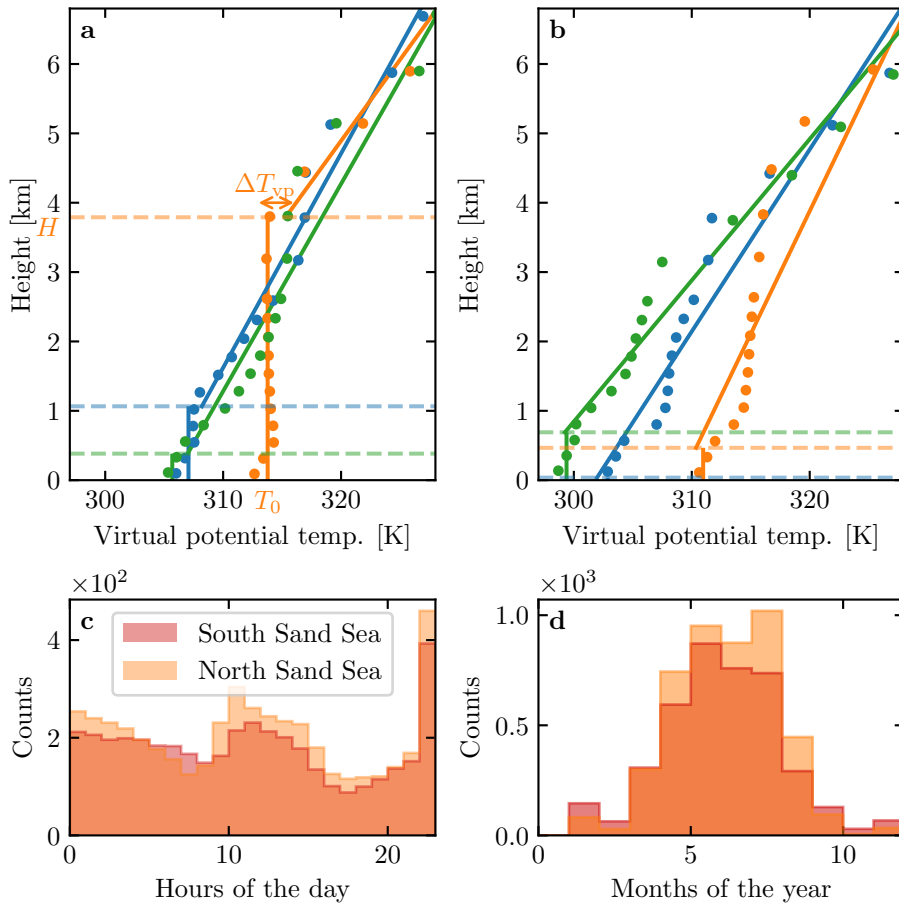


**Fig. S8** **a:** Vertical profiles of the virtual potential temperature at three different times (blue: 29/11/2012 - 1100 UTC, orange: 21/03/2017 - 1200 UTC, green: 21/03/2017 - 2000 UTC) at the South Sand Sea station. Dots: data from the ERA5 reanalysis. Dashed lines: boundary layer height given by the ERA5 reanalysis. Plain lines: vertical (ABL) and linear (FA) fits to estimate the quantities displayed in Online Resource Fig. S9. **b:** Examples of ill-processed vertical profiles at three different times (blue: 2/12/2013 - 2300 UTC, orange: 20/03/2017 - 0000 UTC, green: 14/07/2017 - 1400 UTC) at the South Sand Sea station. **c:** Hourly distribution of ill-processed vertical profiles. **d:** Monthly distribution of ill-processed vertical profiles.

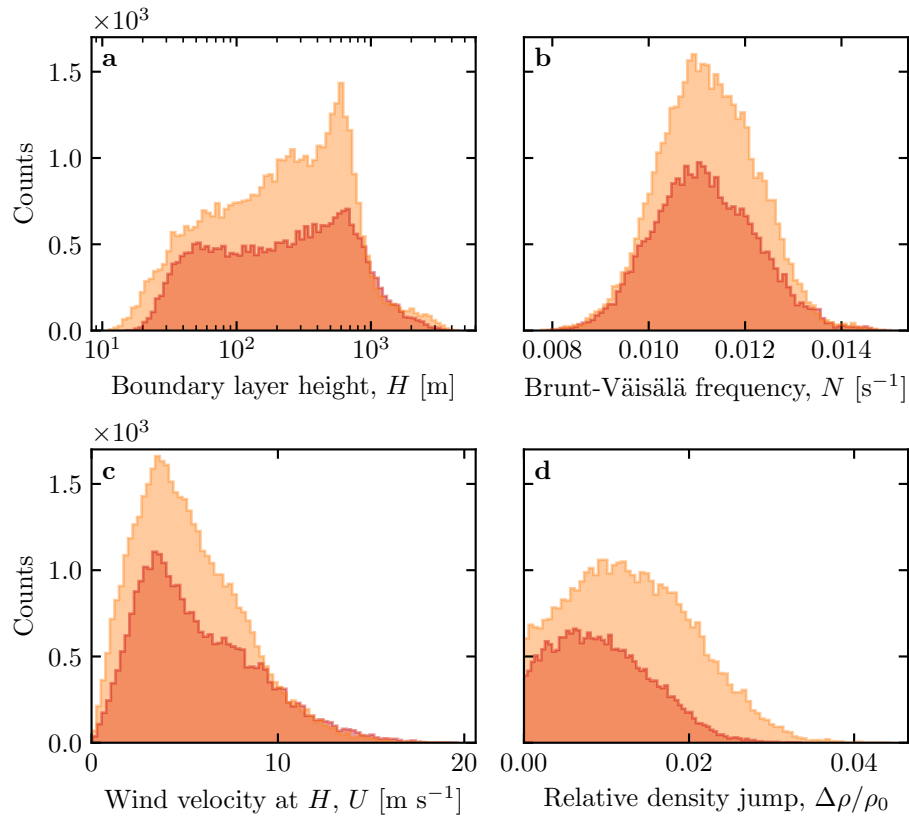


**Fig. S9** Distributions of the meteorological parameters resulting from the processing of the ERA5-Land data for the South Sand Sea (blue) and the North Sand Sea (orange) stations.

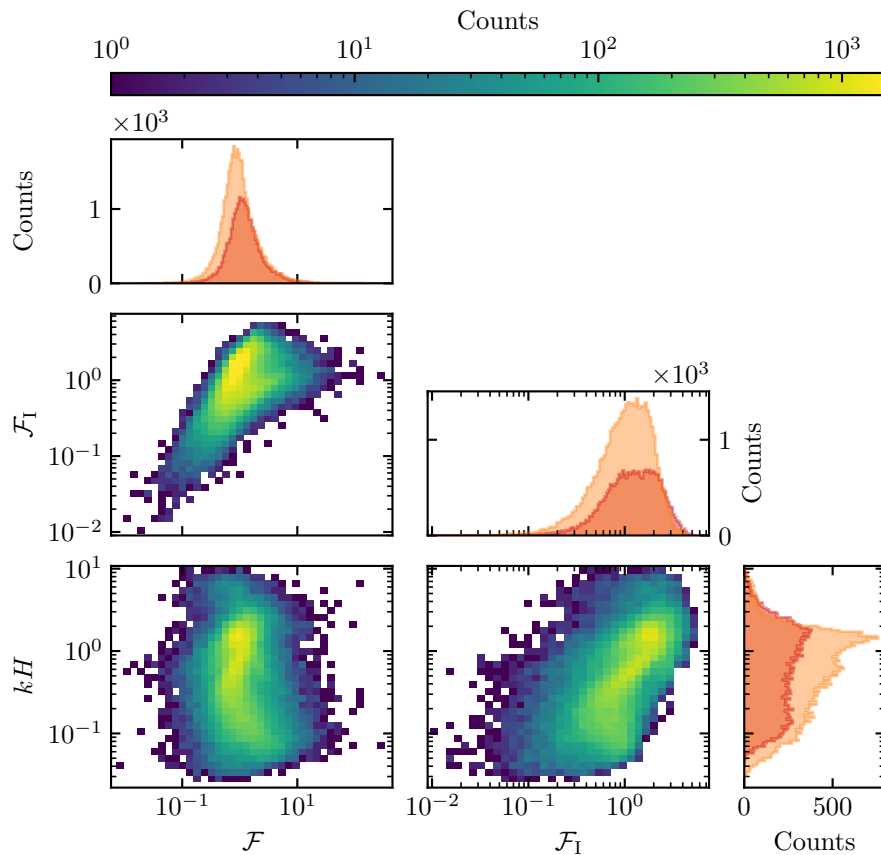


**Fig. S10** Non-dimensional parameters distributions. For the marginal distributions, the orange correspond to the South Sand Sea station, and the blue to the North Sand Sea station.

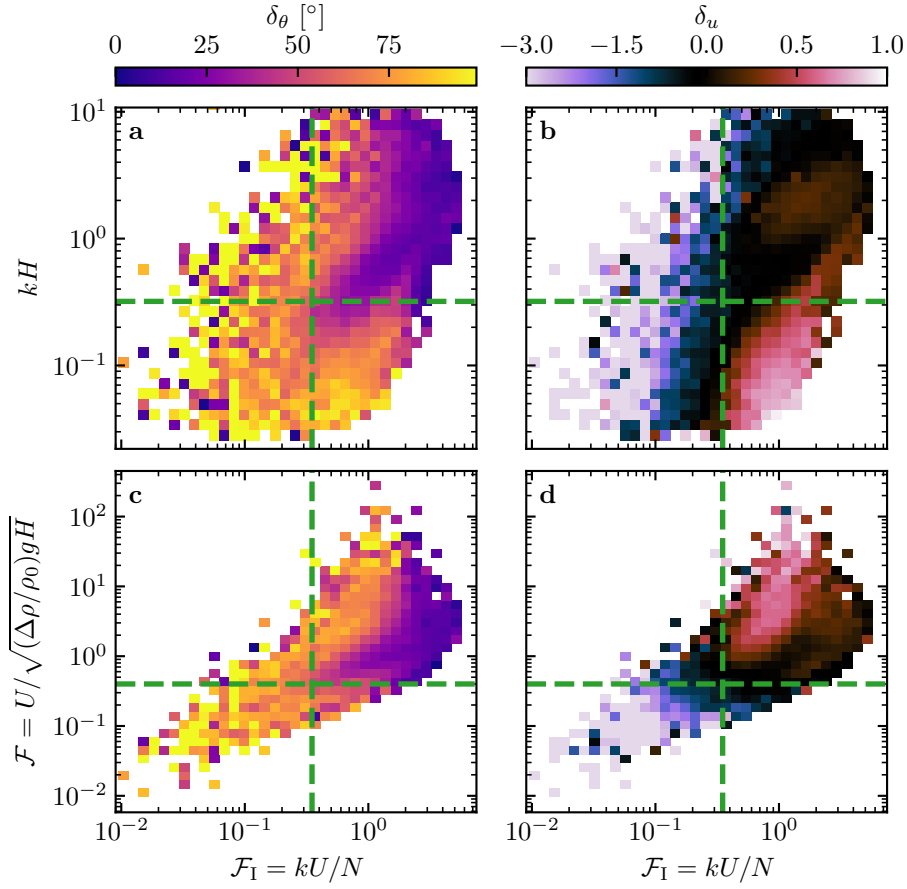


**Fig. S11** Regime diagrams of the wind deviation  $\delta_\theta$  and relative attenuation/amplification  $\delta_u$  in the spaces  $(\mathcal{F}_I, kH)$  and  $(\mathcal{F}_I, \mathcal{F})$ , containing the data from both the North Sand Sea and South Sand Sea stations. Green dashed lines empirically delimit the different regimes. The point density in each bin of the diagrams is shown in Online Resource Fig. S10 – 95% of the data occur in the range  $-1 < \delta u < 1$ . The similar regime diagrams in the space  $(\mathcal{F}, kH)$  are shown in Fig. 8.

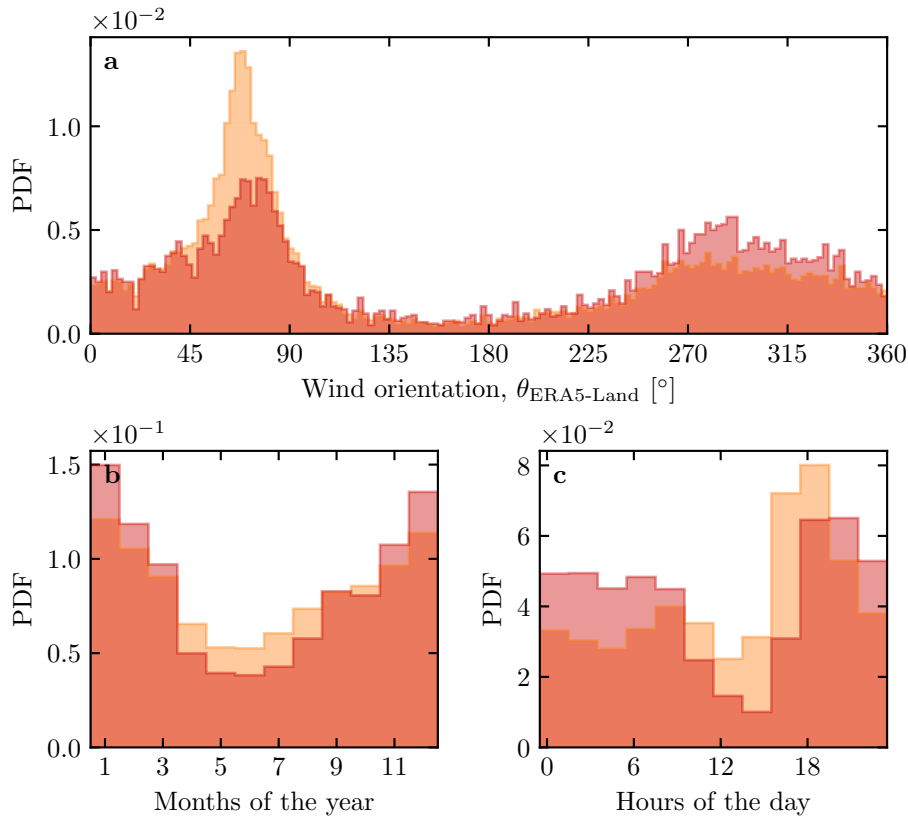


**Fig. S12** Normalized distributions of amplified velocities for the North Sea (blue:  $\delta_u < 0$ , orange:  $\delta_u < -0.5$ ). **a:** Angular distributions. **b:** Monthly distributions. **c:** Hourly distributions.

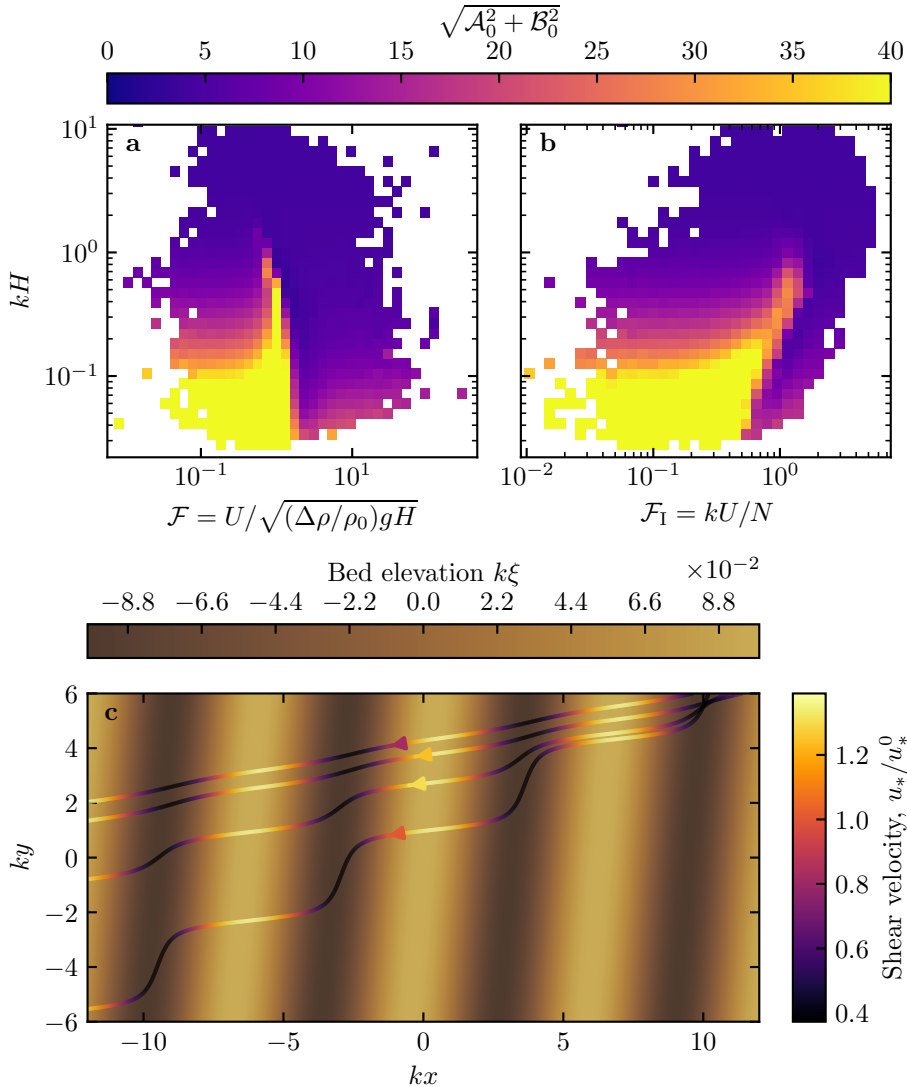


**Fig. S13** Computation of the flow disturbance with the linear model of Andreotti et al. (2009). **a–b:** Magnitude of the hydrodynamic coefficients  $A_0$  and  $B_0$ , calculated from the time series of the non-dimensional numbers corresponding to the ERA5-Land wind data and ERA5 data on vertical pressure levels. **c** Shear velocity streamlines over sinusoidal ridges of amplitude  $k\xi_0 = 0.1$  and for increasing values of  $\sqrt{A_0^2 + B_0^2}$ . From the upper to the lower streamline, values of  $(kH, \mathcal{F}, \mathcal{F}_I, A_0, B_0, \sqrt{A_0^2 + B_0^2})$  are  $(1.9, 0.6, 1.5, 3.4, 1.0, 3.5)$ ,  $(1.5, 0.3, 0.4, 4.8, 1.4, 5.0)$ ,  $(0.1, 3.5, 1.0, 8.6, 0.1, 8.6)$ ,  $(0.5, 0.05, 0.04, 9.6, 2.5, 9.9)$ .

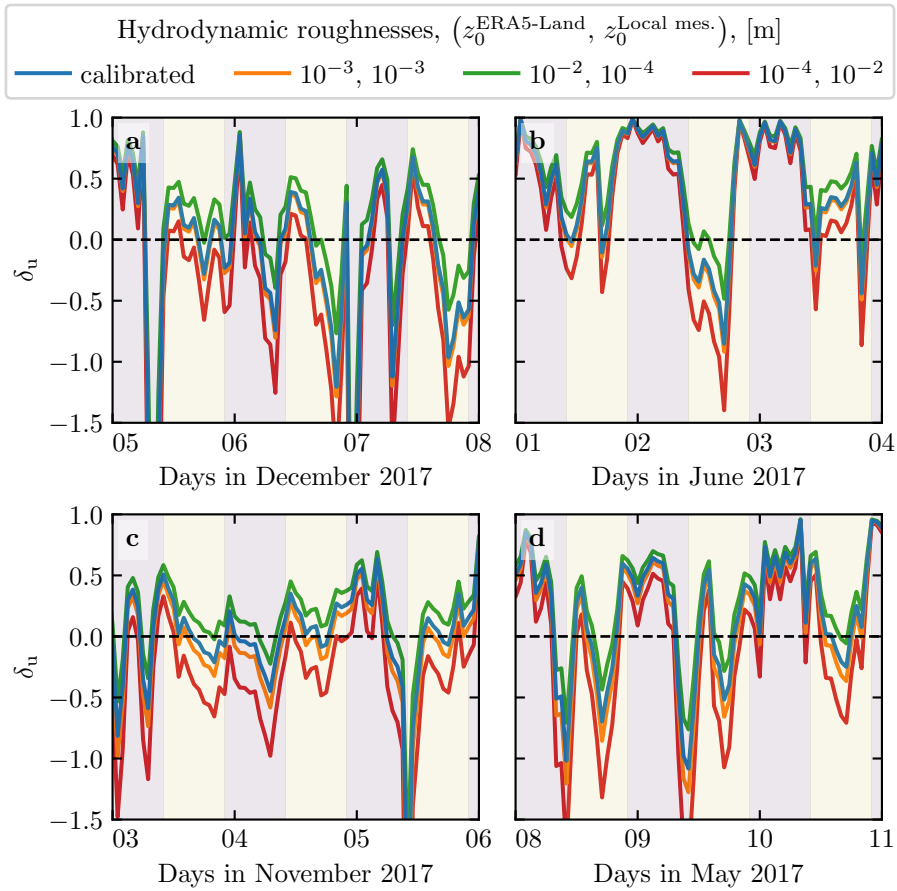


**Fig. S14** Time series of the relative velocity disturbance  $\delta_u$  corresponding to Fig. 5, for different values of the hydrodynamic roughnesses. **a:** North Sand Sea – summer, **b:** North Sand Sea – winter, **c:** South Sand Sea – summer, **d:** South Sand Sea – winter. Note that  $\delta_\theta$  is independent of the choice of  $z_0^{\text{ERA5-Land}}$  and  $z_0^{\text{local}}$ .